TOPICAL REVIEW

Modeling collective charge transport in nanoparticle assemblies

Milovan Šuvakov[1,2] and Bosiljka Tadić[1]

[1] Department of Theoretical Physics, Jožef Stefan Institute, Box 3000, SI-1001 Ljubljana, Slovenia
[2] Institute of Physics, Pregrevica 118, 11080 Zemun-Belgrade, Serbia

E-mail: milovan.suvakov@ijs.si and bosiljka.tadic@ijs.si

Abstract
Mapping the assembled patterns of nanoparticles onto networks (mathematical graphs) provides a way for quantitative analysis of the structure effects on the physical properties of the assembly. Here we review the network modeling of the conduction with single-electron tunneling mechanisms in the assembled nanoparticle films. Simulations of the conduction predict the nonlinear current–voltage curves in different classes of the nanoparticle networks. Furthermore, the numerical analysis reveals how the $I(V)$ nonlinearity is related to the collective charge fluctuations along the conducting paths through the sample, and stresses the role of the topology and quenched charge disorder.

(Some figures in this article are in colour only in the electronic version)

Contents

1. Introduction

Self-assembly processes and the emergent properties of nano-structured systems have introduced some new directions in the recent developments of materials science and technology [1–5]. It has been recognized that the physics and chemistry at the nanoscale differ from that of atoms and bulk material of the same composition [6, 7]. Furthermore, a new route to the macro-world was established via assembly of nano-objects into higher level complex structures and functional devices [8, 9]. The assembled systems of nanoparticles, biomolecules, etc, exhibit a wide

range of fascinating patterns and multiscale structures with emergent physical properties, often incompatible with classical crystalline solids [5]. Some striking examples of assembled 'soft' nanomaterials include supracrystals [10–12], colloidal aggregates [13–16], DNA-guided assemblies [17–21] and bio-nano-heterostructures [22–24], and nanoparticle films on substrates [25–28], which are the subject of this work. These new materials are interesting for various technology applications [2, 3, 29], which naturally require stable and reproducible assembly processes. However, the control of the assembly processes of nano-size objects into higher-order structures and their emergent physical properties still remains a challenging problem for nanoscience and technology. On the other hand, fabrication methods and experimental study as well as the practical applications of various nanomaterials are advancing fast, mainly guided by the accumulating empirical knowledge. However, the full theoretical understanding of the mechanism and potential control of the new properties of nanomaterials is still elusive.

1.1. Complexity of nanoparticle assemblies

The assembly processes are examples of nonlinear driven processes, which are often the subject of various constraints [8, 9, 30]. The spontaneous association of the components with the self-organizing principle, in which local constraints are systematically satisfied, leads to stable multiscale structures. In view of the nonlinear interactions, in complex systems the processes at the micro-scale lead to the resulting behavior on the large scale. In the same spirit, the emergent properties of new nanomaterials consisting of nano-objects as building blocks stems from the nonlinear interactions between these constitutive elements over different scales. To describe the assembled nanomaterials, different theoretical concepts and the appropriate methods are required for the quantum phenomena [6, 31] at the level of the individual nanoparticles and small clusters, on one hand, and for the collective behavior of complex large-scale structures, on the other. Consequently, a unified theoretical approach across all scales is missing. The appropriate numerical modeling and simulations of the physical processes in nanomaterials is, therefore, a method of primary importance. Despite the necessary simplifications and possible technical limitations, numerical modeling helps in understanding dynamical phenomena in the nanoparticle assemblies and provides the way to study the appearance of new properties at the macro-scale. Specifically, within a numerical model one can characterize the physical properties of an assembly by

- computing relevant quantities, which can be defined at different scales and not necessarily be accessible to laboratory experiments;
- exploring a wide range of parameters, which can be used as a guide for experimental analysis and applications;
- determining those parameters which are likely to tune the emergent properties of the ensemble in the desired direction.

In the present work we precisely address these issues in the numerical modeling of charge transport in metal nanoparticle films, which are conducting via single-electron tunneling mechanisms. The phenomenology of conducting nanoparticle films is briefly summarized below. Recently a comprehensive review of the experimental methods which are used to fabricate conducting nanoparticle assemblies and to measure charge transport in these systems was given in [32]. A full range of other methods and the analysis of various properties of nanoparticle assemblies can be also found in [5].

1.2. Phenomenology of the conducting nanoparticle films

Conducting nanoparticle films are usually made by the assembly of noble-metal or semiconductor nanoparticles [32]. Gold nanoparticles, which are often used, and their assemblies exhibit prominent features across different scales [33] and have various applications in microelectronics, optics and biology. Specifically, an isolated gold nanoparticle has electronic and optical properties which are different from the bulk material. Gold nanoparticles can be used for catalysis of certain chemical reactions [33], they can be chemically 'functionalized' to connect to each other along pre-specified directions [34], or coated with polymers, proteins, and DNA molecules, to provide biorecognition binding [35, 22, 36].

Metal nanoparticle films can be produced using different methods [32]. Among well established approaches are lithography [27], drop casting [37] of particles on a substrate, and methods with a liquid support [38, 39], where manipulations with pressure, motion of the liquid and evaporation processes all have an effect of the emergent nanoparticle patterns. In addition, nanoparticle films with a wide variety of structures have been obtained using a non-equilibrium dewetting with a neutral solvent [39, 26, 40] or a charged polymer solution [41], and etching of a polymer matrix with embedded nanoparticles [25]. They range from regular close-packed arrays [42, 43] and nano-networks with well-organized cells [38, 41] to multicellular fractal structures [44] and glassy disordered deposits [45]. (As an illustration, some examples of such nanoparticle films from the literature which inspired our work are shown in figure 1.) Induced by solvent dewetting, effective long-range interactions between the nanoparticles and between the nanoparticles and the substrate are responsible for the spatial structure of the film. The films obtained by different methods also vary in their stability, in view of the binding forces involved, e.g., covalent or hydrogen forces occurring in the case with cross-linking assembly, compared with weak van der Waals forces in the case of liquid support and drop casting methods [32]. Apart from the fabrication procedure and the chemical composition of the nanoparticles, other parameters that may affect the emergent structure are: size (and the dispersion of sizes) of the nanoparticles, and nature of the solvent and the substrate. Additional effects are due to volume fraction of the nanoparticles and steric interactions of the attached thiol chains, or other molecules used to stabilize the metal nanoparticles. In the cross-linking via attached biomolecules, e.g., compatible DNA parts which provide a specific binding, both the nature and the length of the molecules play a role [46, 17–21]. For example, the typical size of Au
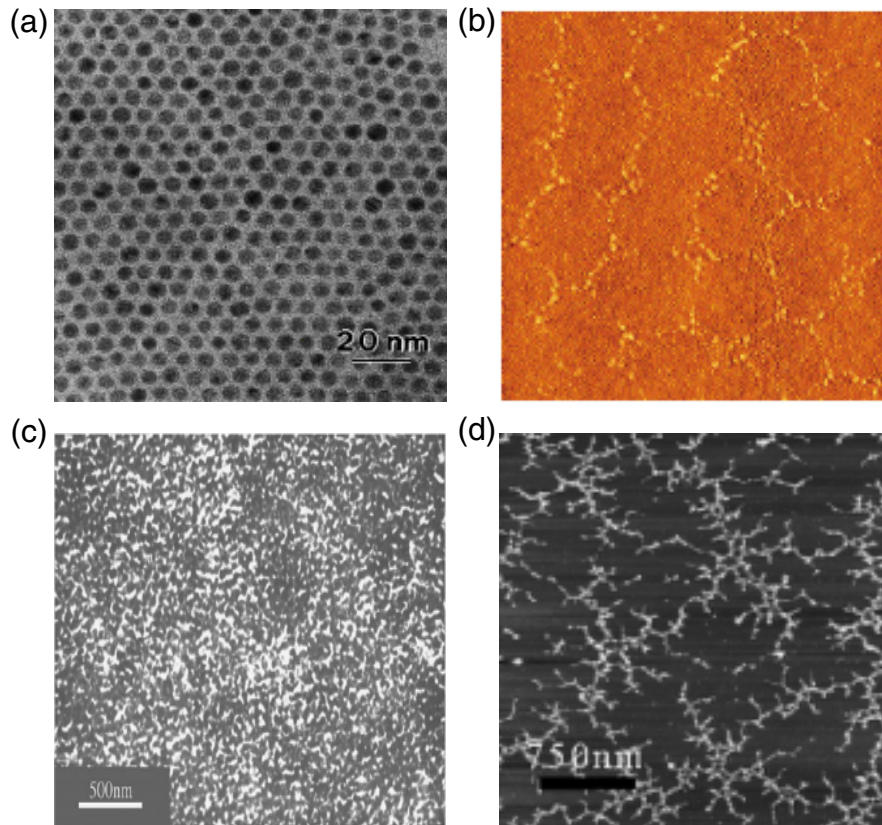
Figure 1. Examples of different patterns of gold nanoparticle films: (a) regular close-packed array (reproduced with permission from [43]. ©2001, Elsevier); (b) polygonal network obtained by drying in a charged polymer solution (reproduced with permission from [41]. ©2004, American Chemical Society); (c) inhomogeneous film made by surface vertical deposition with different velocities (reproduced with permission from [45]. ©2003, IOP Publishing); (d) self-assembled cellular network made by liquid evaporation (reproduced with permission from [44]. ©2010, Oxford University Press).

nanoparticles used in conducting films is in the range 2–7 nm, they are often capped with C_nS molecules, and the distance between pairs of nanoparticles in the assembled film varies between 0.5 and 2.5 nm [32], with the structure depending on the fabrication method and other parameters, as discussed above.

Metallic nanoparticle films on substrates have interesting conduction properties [47–49]. When a positive bias voltage is applied at an electrode the film behaves as a *capacitively coupled system* [50, 51]. The junction between the pair of nanoparticles represents a quantum tunneling resistor–capacitor junction. Due to the small size and resultantly small capacitance of the nanoparticles, charging of a particle by a single electron would increase the particle energy by an amount $e^2/2C \gg k_B T$, an effect known as the Coulomb blockade [52, 49]. Hence *single-electron tunneling* through the labyrinth of junctions in films of small metallic nanoparticles appears as a dominant conduction mechanism [53, 49, 48]. The single-electron processes are highly interesting for new technologies in view of their quantized nature and the absence of thermal dissipation [2].

Conducting nanoparticle films on substrates have been investigated extensively [47, 48, 54, 38, 55–57, 32]. Large amounts of data are now available which suggest a strong connection along the line assembly–structure–conduction-

properties in nanoparticle films. For the above mentioned nanoparticle films the *conductivities* are found in the range [32] from 5×10^{-6} to 1×10^{-2} Ω^{-1} cm^{-1}, varying with the distance between the nanoparticles. One of the most striking features is the occurrence of nonlinearity in current–voltage curves according to the expression

$$I(V) = B \left(\frac{V - V_T}{V_T} \right)^\zeta. \tag{1}$$

It is observed within a range of voltages V just above the threshold voltage V_T, where the electrons penetrating through the pattern of junctions reach the zero-voltage electrode for the first time. The degree of nonlinearity, measured by the scaling exponent ζ, was found to vary considerably with the structure of the film, which in turn is strongly related to the method by which the film was prepared. Experimentally measured values in various nanoparticle films on two-dimensional substrates were found in the range from $\zeta = 2.25$, in a regular close-packed structure [54], to $\zeta = 4.12$, measured in highly inhomogeneous fractal film structures [58]. Furthermore, the presence of fractional charges at the contacts between the nanoparticles and the substrate (charge disorder), the distribution of the size of particles, and the temperature are found to affect the $I(V)$ curves and the threshold voltage in nanoparticle films [54, 59, 38].

Theoretical models of conducting films with the single-electron tunneling between capacitively coupled units have been developed [53, 50, 51, 54–57], with most attention devoted to the study of regular super-lattices and quenched charge disorder [51]. Three regimes can be distinguished, having different dynamic behavior: charge penetration through the sample for $V < V_T$, percolation-type phenomena at the threshold voltage $V \gtrsim V_T$, and another behavior at very large voltages $V \gg V_T$. The nonlinear current–voltage curves in equation (1) can be related to certain dynamic critical phenomena at the threshold voltage V_T. The enhancement of the current for the range of voltages $V \gtrsim V_T$ is attributed to the opening of many conducting paths through the sample, which contribute to the cooperative dynamical behavior of the charge transport. In recent studies [58, 60, 44, 61] we proposed mapping of the capacitively coupled nanoparticle films onto nanoparticle networks (mathematical graphs). Within this approach, which we also use here, films of a general structure can be considered. Moreover, the dynamic behavior along the conduction paths and their topology can be analyzed quantitatively. In addition to topology, related to the conduction paths is the role of quenched charge disorder. Quenched disorder in various dynamical systems was studied extensively during 90s. Here we mention the disorder-induced universal behavior in the problem of optimal paths [62], optimal channel networks [63], and river network dynamics [64], which share some similarity with charge transport in nanoparticle networks.

In this review we present a detailed numerical study based on the network models of single-electron conduction in monolayer nanoparticle films of a general structure. Implementing the single-electron tunneling dynamics on the nanoparticle networks, we perform extensive simulations on different types of structure and analyze the obtained data in view of the driven dynamical systems. The emphasis is on the collective dynamic behavior, which is behind the nonlinear $I(V)$ curves and other observed scaling phenomena, and their relation to the film structure.

2. Single-electron tunneling in systems of nanoparticles

We first describe some basic physical features and parameters of the single-electron tunneling conduction of an isolated junction and of a single nanoparticle, which are basic structural elements of nanoparticle networks.

2.1. Conditions of the Coulomb blockade

Consider a system of metallic nanoparticles arranged on a substrate, separated at small distances from each other and subject to a bias voltage applied to the electrodes across the system. In this system of nano-size conductors, the capacitances are so small that the charging energy due to a single electron $e^2/2C$ may become larger than the thermal energy $k_B T$. Thus the transfer of a single electron between conductors results in a voltage change which creates an energy barrier for further transfer of the electrons—this phenomenon is known as the Coulomb blockade [49]. The barrier persists until the external potential is increased enough to overcome
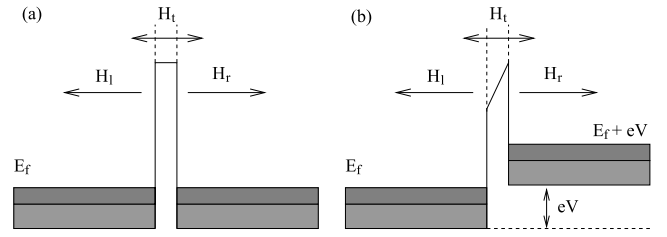

Figure 2. Schematic view of a system with a junction between two metal nanoparticles (a) without and (b) with an applied potential V.

the charging energy. In addition, the charge is well localized on nanoparticles. Using the energy uncertainty relation

$$\Delta E \Delta t \gg h, \tag{2}$$

where the charging energy $\Delta E \sim e^2/C$ and the time for a charge transfer between two nanoparticles is given by $\Delta t \sim R_t C$, we have that the *tunneling resistance* R_t needs to satisfy the relation

$$R_t \gg \frac{h}{e^2} = 25.813 \, \text{k}\Omega. \tag{3}$$

Therefore, single-electron tunneling occurs in the system of nanoparticles when the following conditions are fulfilled:

- the electrostatic energy $e^2/2C \gg$ thermal energy $k_B T$, and
- the tunneling resistance $R_t \gg$ quantum resistance h/e^2.

At room temperature the first condition is satisfied for spherical nanoparticles with a radius in the range $d \lesssim 10$ nm, whereas the tunneling resistance generally depends on the nature of the nanoparticles and the distances between them, as discussed above.

2.2. Electron tunneling at a single junction

When the conditions of the Coulomb blockade are fulfilled, conduction through a junction between an isolated pair of nanoparticles can be considered as a single-electron process within perturbation theory. The transfer Hamiltonian approach for the electron tunneling across a junction, see the schematic view in figure 2, is briefly described in [49]. The two conductors on the left and the right side of the junction, described with the Hamiltonian H_l and H_r, respectively, are independent of each other except for the perturbation H_t, which represents the electron tunneling between them. The total Hamiltonian of the system is given as $H = H_l + H_r + H_t$ and it is assumed that the eigenvectors and eigenvalues of both the left and right Hamiltonians are known:

$$H_l \Psi_l = E_l \Psi_l, \qquad H_r \Psi_r = E_r \Psi_r. \tag{4}$$

Using the fermion creation and annihilation operators of independent many-body states of these two systems, $c_{l,r}^\dagger$ and $c_{l,r}$, one can write the total Hamiltonian as

$$H_0 = H_l + H_r = \sum_{\mathbf{k}_l} E_{\mathbf{k}_l} c_{\mathbf{k}_l}^\dagger c_{\mathbf{k}_l} + \sum_{\mathbf{k}_r} E_{\mathbf{k}_r} c_{\mathbf{k}_r}^\dagger c_{\mathbf{k}_r}, \tag{5}$$

$$H_t = \sum_{\mathbf{k}_l, \mathbf{k}_r} T_{\mathbf{k}_l, \mathbf{k}_r} c_{\mathbf{k}_r}^\dagger c_{\mathbf{k}_l} + \sum_{\mathbf{k}_l, \mathbf{k}_r} T_{\mathbf{k}_r, \mathbf{k}_l} c_{\mathbf{k}_l}^\dagger c_{\mathbf{k}_r}. \tag{6}$$

For a finite temperature the expectation values of the occupation operators $N_{\mathbf{k}_l} = c_{\mathbf{k}_l}^\dagger c_{\mathbf{k}_l}$ and $N_{\mathbf{k}_r} = c_{\mathbf{k}_r}^\dagger c_{\mathbf{k}_r}$ are given by the Fermi–Dirac distribution

$$\langle N_{\mathbf{k}_{l,r}} \rangle = f(E_{\mathbf{k}_{l,r}}) = \frac{1}{1 + e^{(E_{\mathbf{k}_{l,r}} - E_F^{l,r})/k_B T}}. \tag{7}$$

Now we consider tunneling within the single-electron picture in the case when a bias voltage V is applied to the right side (figure 2(b)). It is assumed that the systems remain approximately in thermal equilibrium, so that the one-particle distributions (7) apply, but with different Fermi energies $E_F^r - E_F^l = eV$. The transition rate from an initial state $\mathbf{k}_l$ to a final state $\mathbf{k}_r$ is treated as a scattering process using Fermi's golden rule. The total tunneling rate is then given as a sum over all pairs of the states $\mathbf{k}_l$, $\mathbf{k}_r$:

$$\Gamma^+(V) = \frac{2\pi}{\hbar} \sum_{\mathbf{k}_l, \mathbf{k}_r} |T_{\mathbf{k}_l, \mathbf{k}_r}|^2 f(E_l)(1 - f(E_r))\delta(E_l - E_r), \tag{8}$$

where the matrix elements of the tunneling Hamiltonian are given by $T_{\mathbf{k}_l, \mathbf{k}_r} = \langle \mathbf{k}_r | H_t | \mathbf{k}_l \rangle$. In the case of a relatively high barrier it is usually a good approximation to consider all elements of the tunneling matrix as constant T_0. In addition, the sum over momentum can be converted to a sum over energy. Since the main contribution to the sum comes from the range of energies near the Fermi energy, one can also consider the density of states as a constant both in the left and right particle, D_{l0} and D_{r0}. After one integration the expression for the tunneling rate in equation (8) becomes

$$\Gamma^+(V) = \frac{2\pi}{\hbar} |T_0|^2 D_{l0} D_{r0}$$
$$\times \int_{E_{cm}}^\infty dE\, f(E - E_F^l)[1 - f(E - E_F^r)], \tag{9}$$

where E_{cm} is the higher of two minimal conduction energies. Similar calculations can be done for the tunneling rate in the opposite direction and eventually the net current $I(V)$ through the junction is obtained as the difference

$$I(V) = e[\Gamma^-(V) - \Gamma^+(V)]$$
$$= \frac{2\pi e}{\hbar} |T_0|^2 D_{l0} D_{r0}$$
$$\times \int_{E_{cm}}^\infty dE\, [f(E - E_F^r) - f(E - E_F^l)]. \tag{10}$$

Choosing the Fermi energy of the right nanoparticle as zero energy, we have $E_F^l = -eV$. In the limit when the minimum energy is far below the Fermi energy, the integral in equation (10) can be solved analytically

$$\lim_{E_{cm} \to -\infty} \int_{E_{cm}}^\infty dE\, [f(E) - f(E + eV)] = eV. \tag{11}$$

Hence the $I(V)$ characteristic of a single tunneling junction appears to be ohmic:

$$V = IR_t, \qquad R_t = \frac{\hbar}{2\pi e^2 |T_0|^2 D_{l0} D_{r0}}, \tag{12}$$

where the resistance is given by the *quantum tunneling resistance* R_t.

For our purposes in this work we now consider a generalization of the formula (8) for the case where the transition occurs through a junction between two nanoparticles, which are placed within a large system of N nanoparticles. We can describe the state of such a system with the number of electrons on each nanoparticle $\{n\} \equiv \{n_1, n_2, \ldots, n_N\}$. The change in the energy of the *whole system* before and after a single tunneling process at the $(i \to j)$ junction is then

$$\Delta E_{i \to j} = E\{n_1, \ldots, n_i - 1, \ldots, n_j + 1, \ldots, n_N\}$$
$$- E\{n_1, \ldots, n_i, \ldots, n_j, \ldots, n_N\}. \tag{13}$$

Using the golden rule approximation, the tunneling rate through this junction can be written as

$$\Gamma_{i \to j}(V) = \frac{2\pi}{\hbar} \sum_{\mathbf{k}_s, \mathbf{k}_f} |T_{\mathbf{k}_s, \mathbf{k}_f}|^2 f(E_s)$$
$$\times (1 - f(E_f))\delta(E_s - E_f + \Delta E_{i \to j}), \tag{14}$$

where s and f refer to the initial and the final state of the nanoparticle system. Assuming the same approximations as above, the tunneling rate becomes

$$\Gamma_{i \to j}(V) = \frac{1}{e^2 R_{t,i \to j}} \int_{E_{cm}}^\infty dE\, f(E)[1 - f(E + \Delta E_{i \to j})], \tag{15}$$

where $R_{t,i \to j}$ is given in equation (12), in which now the parameters apply for the particular junction $i \to j$. Using the following property of the Fermi function

$$f(E)[1 - f(E + \Delta E_{i \to j})] = \frac{f(E) - f(E + \Delta E_{i \to j})}{1 - e^{-\Delta E_{i \to j}/k_B T}}, \tag{16}$$

the integral in equation (15) can be solved using (11), which gives

$$\Gamma_{i \to j}(V) = \frac{1}{e R_{t,i \to j}} \frac{\Delta E_{i \to j}/e}{1 - e^{-\Delta E_{i \to j}/k_B T}}. \tag{17}$$

Under the conditions of the Coulomb blockade, equation (17) gives the final expression for the tunneling rate through the junction $(i \to j)$ in the system of N nanoparticles at the potential V. It should be stressed that the energy difference $\Delta E_{i \to j}$ following the tunneling at each junction $(i \to j)$ depends on the energy of the whole system, due to the long-range electrostatic interactions. Other processes may contribute at the local scale of a single junction and modify the local tunneling resistance $R_{t,i \to j}$. In general the resistance may depend not only on the material, size and shape of the nanoparticle, but also on the temperature [65], external magnetic field [66] and the distance between the nanoparticles [67]. Generally, the tunneling resistance increases exponentially with distance [67, 32]. As will be made clear later (see section 4), in our numerical model the tunneling resistance appears as a parameter which enters the timescale of the tunneling processes.

2.3. Single nanoparticle conduction

To illustrate the Coulomb blockade effect in a simple case, here we consider a system consisting of a single nanoparticle on a substrate which is placed between two metal electrodes (shown in figure 3). The tunneling junctions between the electrodes
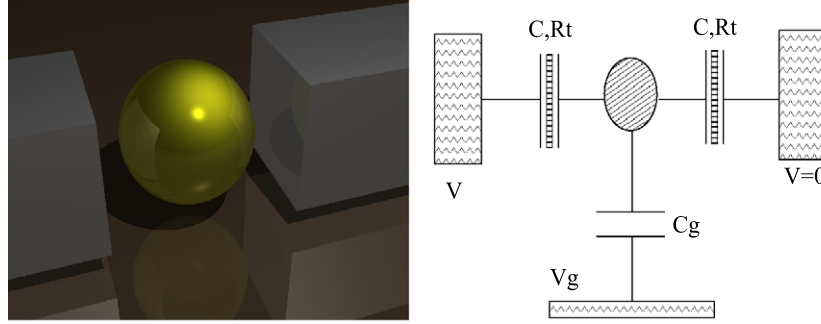
Figure 3. Single nanoparticle on a substrate and between two electrodes. The equivalent circuit of the system under voltage V is shown on the righthand figure.

and the nanoparticle can be characterized by the capacitance C and the tunneling resistance R_t. The substrate (gate electrode) is at the potential V_g and is coupled to the nanoparticle through a capacitor C_g. We assume infinite tunneling resistance along this junction. The equivalent circuit scheme with the bias potential V between the electrodes is also shown in figure 3, right.

For this circuit capacitor charges are given by

$$Q_1 = C(\Phi - V), \qquad Q_2 = C\Phi, \qquad Q_g = C_g(\Phi - V_g), \tag{18}$$

where Φ is the potential of the nanoparticle. During the tunneling process an integer number of electrons n is accumulated on the nanoparticle. Hence the charge of the nanoparticle $Q = -ne$ is expressed as

$$Q = Q_1 + Q_2 + Q_g = C(2\Phi - V) + C_g(\Phi - V_g), \tag{19}$$

from where the potential is found as

$$\Phi = \frac{Q + CV + C_g V_g}{2C + C_g}. \tag{20}$$

Using equation (20) and expressing the energy as $E = \int \Phi(Q)\, dQ + E_e$, where E_e denotes the energy of the electrodes, we can write the electrostatic energy of the system as function of the number of electrons on the nanoparticle:

$$E = \frac{Q^2/2}{2C + C_g} + \frac{Q(CV + C_g V_g)}{2C + C_g} + n^1 eV, \tag{21}$$

where n^1 is the number of electrons on the left electrode. Therefore the energy change associated with the electron tunneling from the left electrode to the nanoparticle is

$$\Delta E_1^+ = \frac{Qe}{2C + C_g} + \frac{e^2/2}{2C + C_g} + \frac{CV + C_g V_g}{2C + C_g}e - eV, \tag{22}$$

and similarly for the tunneling from the nanoparticle to the right electrode

$$\Delta E_2^+ = -\frac{Qe}{2C + C_g} + \frac{e^2/2}{2C + C_g} - \frac{CV + C_g V_g}{2C + C_g}e. \tag{23}$$

Assuming that the system is at zero temperature and that $\Delta E_{1,2}^+ < 0$, equation (17) gives the respective tunneling rates on the two junctions as

$$\Gamma_{1,2} = -\Delta E_{1,2}^+ / R_t e^2. \tag{24}$$

Here the same tunneling resistance $R_t = R$ is assumed for both junctions. The equilibrium state in the tunneling process is attained when the rates are equal, i.e., $\Gamma_1 = \Gamma_2$. Setting the gate potential to zero $V_g = 0$, the charge on the nanoparticle is expressed as

$$Q = \frac{C_g V}{2}. \tag{25}$$

Now, combining the above expressions, we find the current through the system as

$$I(V) = \frac{-\Delta E_{1,2}^+}{Re} = \frac{V}{2R} - \frac{e}{R(C_g + 2C)}. \tag{26}$$

Therefore, in the case of single-electron tunneling through junctions with a single nanoparticle between the electrodes the $I(V)$ dependence remains linear (ohmic conduction). This result serves as one of the benchmark calculations in the numerical implementation (see section 4). As we will show in this work, the nonlinearity in the current–voltage relationship arises due to the spatial arrangement of many nanoparticles between the electrodes in two-dimensional nanoparticle films.

2.4. Electrostatic energy of a nanoparticle network

In this section we briefly describe a generalization of the electrostatic energy and the tunneling rates, to an ensemble of capacitively coupled nanoparticles between the electrodes [51, 53–56]. Here we systematically consider nanoparticle assemblies with a general topology, which is captured by the adjacency matrix of the graph A_{ij} (mapping of a given structure of the nanoparticle assembly onto a mathematical graph as described in section 3). In the derivation of the electrostatic energy and the energy changes due to single-electron tunneling between pairs of nanoparticles in the network, we highlight the main expressions that are relevant for the numerical implementation of the model in section 4.

The expression (19) for the charge of a single nanoparticle is generalized here for the case of a nanoparticle within an ensemble of N nanoparticles as follows

$$Q_i = \sum_j C_{ij}(\Phi_i - \Phi_j) + \sum_\mu C_{i,\mu}(\Phi_i - \Phi_\mu), \tag{27}$$

where Q_i and Φ_i are the charge and the potential of the ith nanoparticle, C_{ij} is the capacitance between the ith and

jth nanoparticle, $C_{i,\mu}$ is the capacitance between the ith nanoparticle and the electrode $\mu \in \{+, -, \text{gate}\}$, and Φ_μ is the potential of the electrode μ. The system of equations (27) for all nanoparticles in the ensemble $i = 1, 2, \cdots N$ can be written in a matrix form and formally solved for the vector $\mathbf{\Phi}$:

$$\mathbf{Q} = \mathbf{M}\mathbf{\Phi} - C_\mu \Phi^\mu \rightarrow \mathbf{\Phi} = \mathbf{M}^{-1}\mathbf{Q} + \mathbf{M}^{-1}C_\mu \Phi^\mu, \quad (28)$$

where $\mathbf{M}$ is the capacitance matrix, with the elements defined by

$$M_{ij} = \delta_{i,j}\left(\sum_k C_{ik} + \sum_\mu C_{i,\mu}\right) - C_{ij}. \quad (29)$$

Then the energy of the nanoparticle ensemble can be written as [51, 53]

$$E = \tfrac{1}{2}\mathbf{Q}^\dagger M^{-1}\mathbf{Q} + \mathbf{Q}\cdot\mathbf{V}^{\text{ext}} + Q_\mu \Phi^\mu, \quad (30)$$

where the potential at each nanoparticle is given by

$$\mathbf{V}^{\text{ext}} = \mathbf{M}^{-1}C_\mu \Phi^\mu, \quad (31)$$

and Q_μ denotes the charge on the electrode μ. In the general case that we consider here, the geometry of the ensemble is determined by the adjacency matrix with the binary elements $\{A_{ij}\}$, which enter the capacitance matrix as follows:

$$M_{ij} = \delta_{i,j}\left(\sum_k CA_{ik} + \sum_\mu C_{i,\mu}\right) - CA_{ij}. \quad (32)$$

We assume for the moment that the capacitances between all pairs of neighboring nanoparticles are equal and given by a constant C.

The system is driven by increasing the potential at one of the electrodes, which causes tunneling of the electrons from the electrode towards nearby nanoparticles and further through the system, by overcoming the Coulomb blockade at the junctions between the nanoparticles. Due to the long-range electrostatic interactions, tunneling of an electron at a single junction ($i \rightarrow j$) leads to energy changes over an extended area. Technically, these effects are included via the inverse capacitance matrix in the first two terms of equation (30). For our numerical purposes, here we write separately the energy changes in these two terms, which we denote as $\Delta E^{(1)}$ and $\Delta E^{(2)}$, respectively.

Tunneling of a single electron from the nanoparticle a to the neighboring nanoparticle b causes changes in the vector of charges as $Q_i' = Q_i + \delta_{bi} - \delta_{ai}$, where δ_{ai} is the Kronecker delta. Hence the change in the first energy term $\Delta E^{(1)}(a \rightarrow b) \equiv E^{(1)'} - E^{(1)}$ can be written as follows:

$$\Delta E^{(1)}(a \rightarrow b)$$
$$= \tfrac{1}{2}\sum_{ij}(Q_i + \delta_{bi} - \delta_{ai})M_{ij}^{-1}(Q_j + \delta_{bj} - \delta_{aj})$$
$$- \tfrac{1}{2}\sum_{ij}Q_i M_{ij}^{-1}Q_j. \quad (33)$$

Using the property of the capacitance matrix that $M_{ij}^{-1} = M_{ji}^{-1}$, the expression (33) becomes

$$\Delta E^{(1)}(a \rightarrow b) = \sum_i Q_i(M_{ib}^{-1} - M_{ia}^{-1})$$
$$+ \tfrac{1}{2}(M_{aa}^{-1} + M_{bb}^{-1} - M_{ab}^{-1} - M_{ba}^{-1}). \quad (34)$$

Similarly, we find the change in the second energy term $\Delta E^{(2)}(a \rightarrow b) \equiv E^{(2)'} - E^{(2)}$ following the tunneling of an electron from $a \rightarrow b$:

$$\Delta E^{(2)}(a \rightarrow b) = \sum_i(Q_i + \delta_{bi} - \delta_{ai})V_i^{\text{ext}} - \sum_i Q_i V_i^{\text{ext}}$$
$$= V_b^{\text{ext}} - V_a^{\text{ext}}. \quad (35)$$

Note that the tunneling process is biased in the direction of decreasing potential, however tunnelings in the reverse direction may occur and need to be considered.

Both energy terms have a contribution due to the tunneling processes between the electrodes and the nanoparticles in their vicinity. For example, for a single-electron tunneling between the electrodes (denoted as $\pm$) and the nanoparticle a, causing the charge update $Q_i' = Q_i \pm \delta_{ai}$, the energy changes in the two terms are

$$\Delta E^{(1)}(a \leftrightarrow \pm)$$
$$= \tfrac{1}{2}\sum_{ij}(Q_i \pm \delta_{ai})M_{ij}^{-1}(Q_j \pm \delta_{aj}) - \tfrac{1}{2}\sum_{ij}Q_i M_{ij}^{-1}Q_j$$
$$= \pm\sum_i Q_i M_{ia}^{-1} + \tfrac{1}{2}M_{aa}^{-1}, \quad (36)$$

and

$$\Delta E^{(2)}(a \leftrightarrow \pm) = \sum_i(Q_i \pm \delta_{ai})V_i^{\text{ext}} - \sum_i Q_i V_i^{\text{ext}}$$
$$= \pm V_a^{\text{ext}}. \quad (37)$$

For practical purposes, introducing the variable

$$V_c \equiv \sum_i Q_i M_{ic}^{-1}, \quad (38)$$

we can then write the expressions (33) and (36) in more closed forms:

$$\Delta E^{(1)}(a \rightarrow b)$$
$$= V_b - V_a + \tfrac{1}{2}(M_{aa}^{-1} + M_{bb}^{-1} - M_{ab}^{-1} - M_{ba}^{-1}), \quad (39)$$

and

$$\Delta E^{(1)}(a \leftrightarrow \pm) = \pm V_a + \tfrac{1}{2}M_{aa}^{-1}, \quad (40)$$

which are suitable for the numerical implementation. In summary, after the tunneling process occurs, the updated variable V_c' can be calculated from the previous one as follows:

$$a \rightarrow b: \qquad V_c' = V_c + M_{bc}^{-1} - M_{ac}^{-1}, \quad (41)$$

$$a \leftrightarrow \pm: \qquad V_c' = V_c \pm M_{ac}^{-1}. \quad (42)$$

For simplicity, in the numerical model we take the capacitance $C_{i,\text{gate}} = C_\text{g}$ between a nanoparticle and the substrate (gate electrode) to be equal for all nanoparticles. Similarly, the capacitances between the $\pm$ electrodes and the neighboring nanoparticles is taken to be the same as the interparticle capacitance C. In the limit when $C \ll C_\text{g}$ the diagonal elements of the capacitance matrix $\mathbf{M}$ are much larger compared to the off-diagonal elements. The off-diagonal elements of the inverse matrix $\mathbf{M}^{-1}$ fall off exponentially, which allows one to use the nearest-neighbor approximation [51], specifically for calculations of the quantities V_c in equations (41) and (42) in this limit.

In our numerical model in section 4, for simulations of the tunneling processes in the nanoparticle assemblies, we will systematically refer to equations (35) and (39) for tunneling between pairs of nanoparticles ($a \rightarrow b$), and to equations (37) and (40) when the tunneling occurs between a nanoparticle and the electrodes ($a \rightarrow \pm$). As will be made clear later, in our numerical implementation we can treat the most general case including a range of values of the capacitances C and C_g beyond the limit $C \ll C_g$. In addition, a nonuniform distribution of the capacitances C_{ij} and $C_{i,\text{gate}}$ can be easily implemented. In order to clearly determine the role of topology in the electron transport through complex nanoparticle networks, we will discuss in detail cases with only two constant capacitances, C and C_g, as introduced above.

Since the early work of Middleton and Wingreen [51], several types of theoretical model were considered in the efforts to understand the charge transport through nanoparticle arrays and the occurrence of scaling at the threshold voltage [57, 54, 56]. The numerical implementation of these models are chiefly related to regular arrays, possibly with charge disorder and weak structural disorder. It should be stressed that in this work we consider a generalization of the Middleton and Wingreen [51] model of single-electron tunneling, in which we incorporate the most general structure of the assembly via the concept of the nanoparticle network topology. Hence, we recover the results of [51] in the limit when the networks with a strictly regular structure (hexagonal or triangular) are considered. Another approach based on molecular dynamics simulations was proposed in [57]. The equations of motion are numerically solved for a given number of mobile charges, interacting via a Coulomb potential on a regular array. The charges are subject to a driving force, which is directly related to the applied voltage, and local traps, which mimic the nonlinear threshold dynamics in the Coulomb blockade conditions. The traps are implemented as local threshold voltages. Although the theoretical concept of random local voltages is much simpler compared to the single-electron tunneling processes explained above, it gives an insight into the conduction of disordered arrays. The charge disorder is given by a Gaussian distribution of threshold voltages over sites, while the structural disorder is introduced by randomly selected areas where infinite voltage thresholds apply to prevent the charge flow. Tracing the exact paths of the moving charges in the molecular dynamics simulations reveals the role of disorder in the charge transport.

3. Planar graph models of nanoparticle assemblies

As mentioned in section 1, one of the objectives of this review is to substantiate the structure–dynamics interdependences in nanoparticle films using theoretical arguments and quantitative analysis. For this purpose, we describe the arrangement of the nanoparticles by mapping them onto networks and using graph theoretical methods. In recent years there has been a great interest in the study of evolving networks and their applications in physics and other areas of research (see recent review [68]). In particular, graphs with a short diameter ('small-world' networks) and scale-free networks with a

power-law connectivity [69, 68] have found many practical applications in the study of complex dynamical systems, and in particular, the transport processes on networks [70, 71]. In order to model the conducting nanoparticle films by networks, we note the following: first, the basic elements of the network, *nodes* and *links*, are suitably identified as *nanoparticles* and *tunneling junctions*, respectively. Furthermore, the interesting realizations of conducting nanoparticle films are extended structures with a large distance between the electrodes, and the films are usually made up of monolayers of nanoparticles on the substrates. This implies an embedded planar graph structure. The self-assembled nanoparticle films often appear to have an inhomogeneous structure with individual particles or cells of particles attached to each other (see for example figure 1). In modeling realistic structures of nanoparticle films by networks several approaches can be used. Here we describe two such approaches: (a) computer generated planar graphs of a topologically matching structure, and (b) data driven models using the actual particle positions on the substrate. Directly modeling the assembly processes of the interacting nanoparticles is yet another approach, which belongs to a broad area known as *colloidal aggregation* (see recent review in [16]). Due to limited space, we will not discuss this approach in any detail here. Some examples of nanoparticle films emerging in aggregations with biorecognition binding potential, together with details of the numerical implementation can be found in [60, 44].

3.1. Grown cell-aggregated structures

Recently we have introduced a model [72] to grow *planar graphs* with a *cellular structure*, which match topologically some of the nanoparticle films in [73, 38, 41]. In the model, the aggregation of small cycles (or cells) of nanoparticles is controlled by two parameters. Starting with a single cell, the graph grows by attaching a cell of length n_p to the boundary of the already existing part of the graph. The exact attachment rules are explained below. During the attachment we observe two types of constraints: first, we preserve the planarity of the graph at each growth step. In addition, for the reasons to be made clear later, here we consider only graphs with a fixed number of links per node $k = 3$, which is thus fulfilled everywhere in the interior of the graph [72]. Therefore, the distribution of cell sizes $f(n_p)$ is defined for $n_p \geqslant 3$, for a non-clustered graph we fix $f(3) = 0$. Moreover, the planar graph of N nodes and E links obeys Euler's law: $N_p + N = E + 1$, where N_p is the number of polygons. Homogeneous plane-filling structures are of special interest for us [74]. For this class of graphs, the majority of nodes are in the interior of the graph, i.e., are nodes with degree $k = 3$. Thus $3N \approx 2E$ and Euler's law gives

$$6N_p = 2E + 6. \tag{43}$$

For a large system with distribution of cell sizes $f(n_p)$ we have

$$N = N_p \sum_{n_p} \frac{n_p f(n_p)}{3}, \tag{44}$$

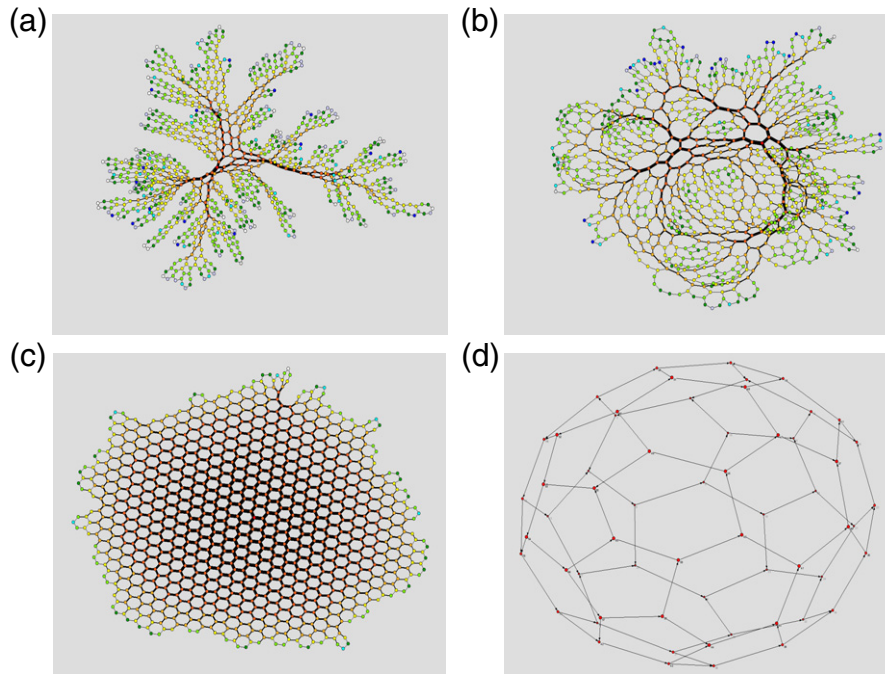$$E = N_p \sum_{n_p} \frac{n_p f(n_p)}{2}. \tag{45}$$

Figure 4. Examples of the emergent cell-aggregated graphs. Open structures obtained for (a) $\mu_2 = 0.5$, $\nu = 0$; (b) $\mu_2 = 2$, $\nu = 1$; (c) $\mu_2 = 0$ (hexagons only), $\nu = 1$. Example of a closed C_{60}-like structure (d). ((a) and (b) reprinted with permission from [72]. ©2006, Springer Science + Business Media.)

Substituting the second relation into (43), we have $6N_p = N_p \sum_{n_p} n_p f(n_p) + 6$. Then for $N_p \gg 1$ one can find that the average cell size is equal to six

$$\langle n_p \rangle \equiv \sum_{n_p} n_p f(n_p) = 6. \qquad (46)$$

Inspired by the cellular structures obtained in the laboratory [38, 41], in this work we use the log–normal distribution of the cell sizes

$$f(n_p) = \frac{1}{s\sqrt{2\pi}\, n_p} \mathrm{e}^{-\frac{\ln^2 n_p/n_0}{2s^2}}, \qquad (47)$$

around an average hexagonal structure. With the condition (46) the number of independent parameters in equation (47) is reduced

$$\langle n_p \rangle = 6 \Rightarrow n_0 = 6\mathrm{e}^{-s^2/2}, \qquad s^2 = \ln\left(1 + \frac{\mu_2}{36}\right). \quad (48)$$

The second central moment μ_2 remains as the control parameter in our model. The other parameter is related to the attachment affinity of cells (defined below). At each growth step a new cell, with size taken from the distribution $f(n_p)$, is attached to the graph boundary according to the following rules.

 (i) In the aggregation only nodes with degree $k = 3$ can be closed inside the graph.
 (ii) A new edge (link) can be assigned only to nodes with degree $k = 2$.
(iii) A potential nesting place is searched as an array of nodes on the graph boundary with the degree $k = 3$ limited

with two nodes of the degree $k = 2$. The nested part of the cell is identified with the nodes of the nesting string. Therefore, the number of nodes to be added is $n = n_p - l$, where l is the length of the nesting string. We select the nesting place with probability $p \sim \mathrm{e}^{-\nu n}$, where the parameter ν plays the role of the chemical potential for the addition of n new nodes.

In figure 4 some emergent structures are shown, depending on the parameters μ_2 and ν. Note that when $\nu = 0$ all nesting places on the graph boundary are equally probable. Consequently, for small values of ν the emergent structures appear to have a long fractal boundary. The situation resembles the more familiar diffusion-limited aggregation, however, here the cells of particles are aggregated instead of single particles! In the case when ν is large, more compact plane-filling structures occur, with the length of the boundary proportional to the square root of the number of nodes. In the special case for $\mu_2 = 0$ the aggregates consist of hexagonal cells only, as shown in figure 4(c). Depending on the model parameters and the course of the growth process, it may occur that after some number of steps no nodes with degree two remain. In that case the structure is closed for further growth (according to rule 2) and the algorithm stops. Various forms of closed structures can be grown in this way [61]. With the right mixture of cells, one can obtain a closed structure of the C_{60}-like topology, shown in figure 4(d). In the study of conduction processes we focus on open plane-filling structures. The electrodes are placed on selected areas along the graph boundary. Here we summarize certain topological properties of these graphs, namely the path lengths and the betweenness
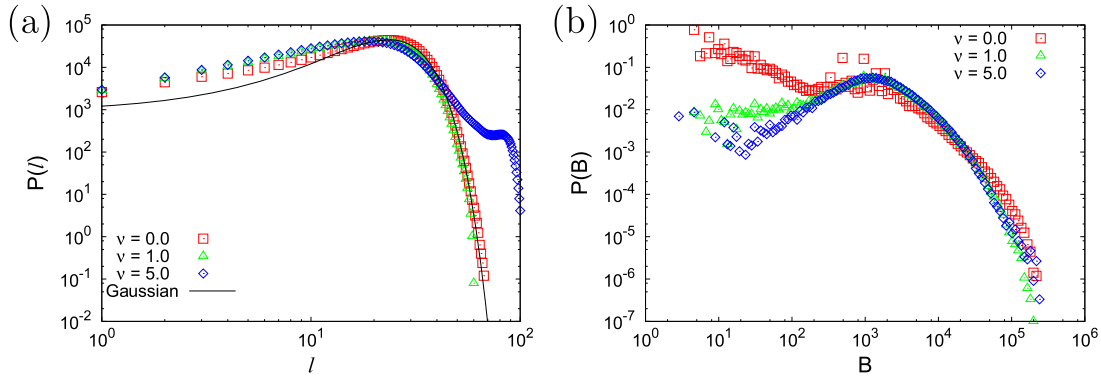
Figure 5. Topological properties of the emergent cell-aggregated networks: (a) distribution of the lengths of the shortest paths on the networks for fixed $\mu_2 = 0.5$ and several values of ν. Solid line represent a Gaussian with $l_0 = 23.5$ and $\sigma = 8.37$. (b) Distributions of the betweenness centrality of the links. (Data from [72].)
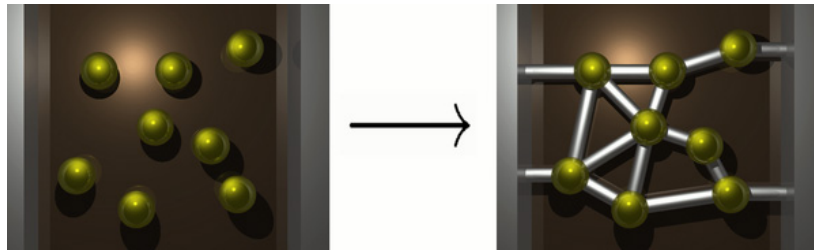

Figure 6. Construction of the conduction network from known positions of the nanoparticles and the electrodes: the junctions along which the tunnelings are possible are indicated by the links.

centrality of nodes (or links), which are important for the conduction process (see also [72, 75]).

Shortest path length between a pair of nodes s and t is given as the number of links (nodes) occurring along a topological shortest path [76] from s to t on the graph.

Betweenness centrality is a topological measure of the importance of a node (or a link) on the graph. It is defined by [76, 77]

$$C_{\mathrm{B}}(v) = \sum_{s \neq v \neq t} \frac{\sigma_{st}(v)}{\sigma_{st}}, \qquad (49)$$

where σ_{st} is total number of *shortest paths* between the nodes s and t, and $\sigma_{st}(v)$ is number of these paths which pass through the node v. Betweenness of links is defined in an analogous way. For inhomogeneous networks the distribution of the betweenness of nodes can be substantially different from that for links. In our case, however, there is no difference because of the fixed degree $k = 3$ of the nodes.

In figure 5 we show the distributions of the lengths of the shortest paths and the distributions of betweenness of links for networks grown with a fixed parameter $\mu_2 = 0.5$ and several values of the parameter ν. The size of these networks is $N \approx 1000$ nodes. The distributions are averaged over 100 sample networks for each set of the parameters. The distributions of betweenness at the small scale strongly depend on the parameter ν, related to different graph boundaries. Similar conclusions hold for other μ_2 values (not shown). The meaning of the topological betweenness is illustrated for the links of the graphs in figure 4: the width of each link represents the computed betweenness of that link on the graph. For this type of network the strongest lines connect the nodes with the

largest centrality measure. These links therefore can be the most important for charge transport through the graph.

3.2. Nano-networks from the empirical data and assembly models

Another type of network model, which we use for the simulations of charge transport, is based on data on the positions of the nanoparticles on the substrate. We assume that the positions of the nanoparticles are known, e.g., either via STM measurements or by statistical estimates based on the parameters of the deposition process, or from the simulations of the assembly process itself. In order to make a reasonable nanoparticle network based on such data, it is crucial to take into account that the tunneling resistance increases (conductivity decreases) exponentially with distance between the nanoparticles [49, 32]. Consequently, the probability of electron tunneling decays and virtually vanishes at large distances. Taking a sharp threshold, a distance called the tunneling radius r, is a parameter which determines the tunneling proximity of the nanoparticles in the ensemble. In real films, r can be of the order of a few nanometers, depending in part on the type of nanoparticles [32]. The nanoparticle film network is then constructed by inserting a link $A_{ij} = 1$ between each pair of nanoparticles (i, j) which are separated by less than the tunneling radius r from each other. Otherwise, $A_{ij} = 0$. Also, when the shape and the positions of the electrodes are known, we connect the nanoparticles with an electrode if the distance between them is smaller than the tunneling radius r. The procedure is illustrated in figure 6. In our numerical approach, the tunneling radius r appears as
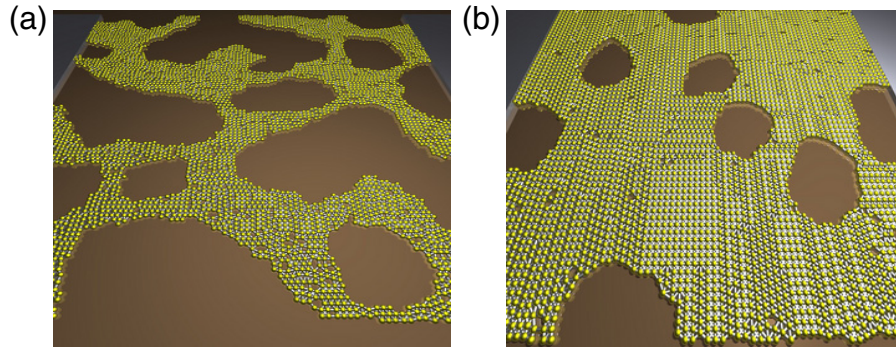
Figure 7. A three-dimensional rendering of the nanoparticle networks used in the charge transport simulations. Networks are constructed using the exact coordinates of the nanoparticles from [26]. The two structures correspond to different nanoparticle coverage (a) 40%, NNET1, and (b) 80%, NNET2. (Reprinted by permission from [58]. ©2007, American Chemical Society.)
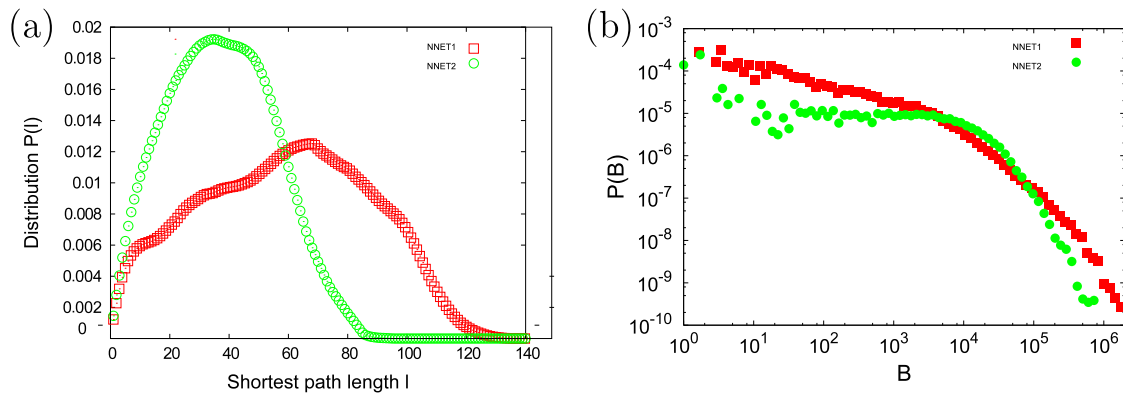

Figure 8. Distribution of the lengths of shortest paths (a) and betweenness centrality (b) for the nanoparticle networks NNET1 and NNET2 shown in figure 7.

an additional parameter of the network model. Two examples of the nanoparticle networks constructed with these rules, and used in the simulations of charge transport in section 5, are shown in figure 7. The coordinates of the nanoparticles are taken from the simulations of nanoparticle assembly with dewetting using the model described in [78, 26]. The two structures correspond to different values of nanoparticle coverage, 40% (NNET1) and 80% (NNET2), respectively. As discussed in [58], the properties of these assemblies are closely related to those observed in the experiment [26].

The results of topological analysis of these two networks are shown in figure 8. The distribution of the lengths of the shortest paths, figure 8(a), shows a strong dependence on the coverage. The network NNET1 with smaller coverage appears to have large inhomogeneities in the structure. Consequently, the structure of its shortest paths is changed, and the average length of the paths increased in comparison with the more compact network NNET2. The structural inhomogeneity also affects the betweenness centrality of the links, figure 8(b). For the compact network NNET2 the distribution of betweenness exhibits some similarity to the one for cell-aggregated networks in figure 5(b). On the other hand, the topological inhomogeneity with the large voids in NNET1 induces a number of 'bottle necks'—links with large betweenness centrality, leading to the tail in the

distribution. The topology of conduction paths, discussed below in section 5, is closely related to the shortest paths on these networks.

4. Numerical model

4.1. Implementation of the algorithm

Our implementation of the single-electron conduction model is based on the analytical expressions derived in section 2.4. We start with a specified nanoparticle network, given by its adjacency matrix A_{ij}, which is constructed as explained above. Choosing the positions of the electrodes, we also connect the electrodes with the adjacent row of nanoparticles found within a tunneling radius r. We assume that at the initial time $t = 0$ the system is not charged (all charges at the nanoparticles Q_i are set to zero) and apply a constant biased potential Φ_μ on the electrodes. In the initialization we calculate the inverse of the capacitance matrix $\mathbf{M}$ and the components of the vector $\mathbf{V}^{ext}$, given by equations (32) and (31), respectively.

The algorithm is based on successive steps in time, where each step corresponds to one tunneling event. Using the procedure described in section 2.4, in each step we calculate the energy change for an attempted tunneling along every junction ($i \rightarrow j$) in the network, including the junctions with the electrodes. From the computed energy change, we then

calculate the tunneling rate Γ_{ij}, in view of the expression (17). We implement continuous time dynamics by introducing the tunneling time distribution

$$f_{ij}(t) = \Gamma_{ij} e^{-\Gamma_{ij} t}. \qquad (50)$$

Technically, the tunneling time t_{ij} is then a random number generated from this distribution. Calculating the cumulative distribution

$$F_{ij}(t) = 1 - e^{-\Gamma_{ij} t} \qquad (51)$$

and solving the equation $F_{ij}(t_{ij}) = x$ for t_{ij}, with a uniform random number $x \in [0, 1]$, gives the tunneling time for the process associated with the computed energy change $\Delta E(i \to j)$:

$$t_{ij} = -\frac{\log(1-x)}{\Gamma_{ij}}. \qquad (52)$$

Note that Γ_{ij} may also change with time, following the tunneling events. Thus the appropriate distribution of the tunneling times is given by an integral, i.e.,

$$f_{ij}(t) = \Gamma_{ij}(t') e^{-\int_0^t \Gamma_{ij}(t')\,dt'}, \qquad F_{ij}(t) = 1 - e^{-\int_0^t \Gamma_{ij}(t')\,dt'}, \qquad (53)$$

leading to an integral equation for t_{ij}:

$$\int_{t_{k_0}}^{t_{ij}} \Gamma_{ij}(t')\,dt' = -\log(1-x). \qquad (54)$$

In our case the tunneling rates are part-by-part constant functions between the tunneling event. Therefore we can convert the integral (54) into the sum over time intervals between successive tunnelings, which occur at unevenly spaced times t_k, $k = 1, 2, 3, \ldots$. Consequently, assigning a uniform random number x_{ij} to each junction, we determine the time delay Δt_{ij} until the next tunneling at a particular junction $(i \to j)$ by solving (54):

$$\Delta t_{ij} = \frac{-\log(1-x_{ij}) - \sum'_{k > k_0} \Delta t_k \Gamma_{ij}(t_k)}{\Gamma_{ij}(t)}, \qquad (55)$$

where the sum is over all tunnelings in the entire system since the last tunneling event occurring at the junction $(i \to j)$ at the moment t_{k_0}. Δt_k denotes the intervals between such events, and their effects on the tunneling rate at the junction $(i \to j)$ are taken via $\Gamma_{ij}(t_k)$. Solving the set of equations (55) for all junctions in the network, we then find the junction which has minimal Δt_{ij} and perform the tunneling along that junction. Following the tunneling event, we update the vectors $\mathbf{Q}$, $\mathbf{V}_c$ for the whole system and also assign a new random number x_{ij} to that junction. Then the whole process is repeated to find the junction at which the next tunneling will occur, and so on.

In this stochastic process the electrons start entering the system of nanoparticles when the bias voltage is applied at the electrodes. The number of electrons on a nanoparticle Q_i increases in time, depending on the actual value of the voltage. For each ramp of the voltage, the number of electrons at each nanoparticle inside the system stabilizes after some relaxation time. For voltages below a threshold V_T, the charged nanoparticles form a pattern with a moving front.
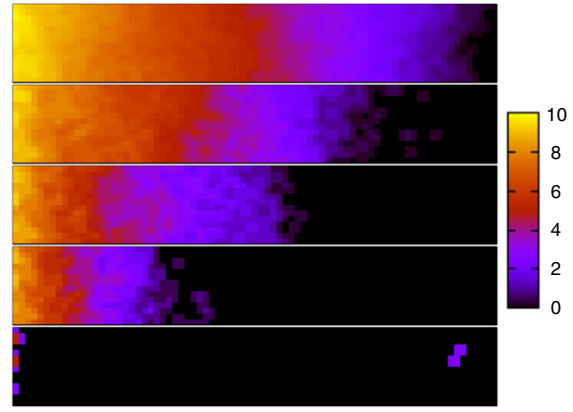

Figure 9. Moving fronts of charges in strips of regular nanoparticle arrays shown for several values of the voltage below the threshold $V < V_T$, increasing from the bottom to top. (Reprinted with permission from [60], ©IOP Publishing.)

The situations for several values of the voltage are illustrated in figure 9 for the case of strips with a regular nanoparticle array. The moving front reaches the zero-voltage electrode when $V \sim V_T$, depending on the structure of the network and distance between the electrodes. Then the current can be detected as the number of electrons tunneling to the electrode per time unit.

Schematically, the main steps in the algorithm are:

```
Input: graph, parameters
Calculate capacitance and
    inverse capacitance matrix
Initialize vectors Q, Vc, V+
    with zeros
Initialize time t=0
While(V+ <  V_{max})
While(enough sampled data)
  Calculate vector Vc
  Calculate energy change for
     all junctions
  For each link
    t(i,j)=next random from
       distribution pij(t)
  End For
  Process the tunneling with
     smallest time t(i,j)
  Increment time t=t+t(i,j)
  If(relaxation is done)
    Sample data of interest
  End If
End While
Increase V
End While
```

We use LU decomposition to calculate the inverse capacitance matrix. This algorithm require N^3 computational steps, where N is the size of the matrix, in our case given by the number of nanoparticles. The rest of the code requires N^2 operations per each tunneling event. Hence, the algorithm complexity is $O(N^3 + MN^2)$, where M denotes the number
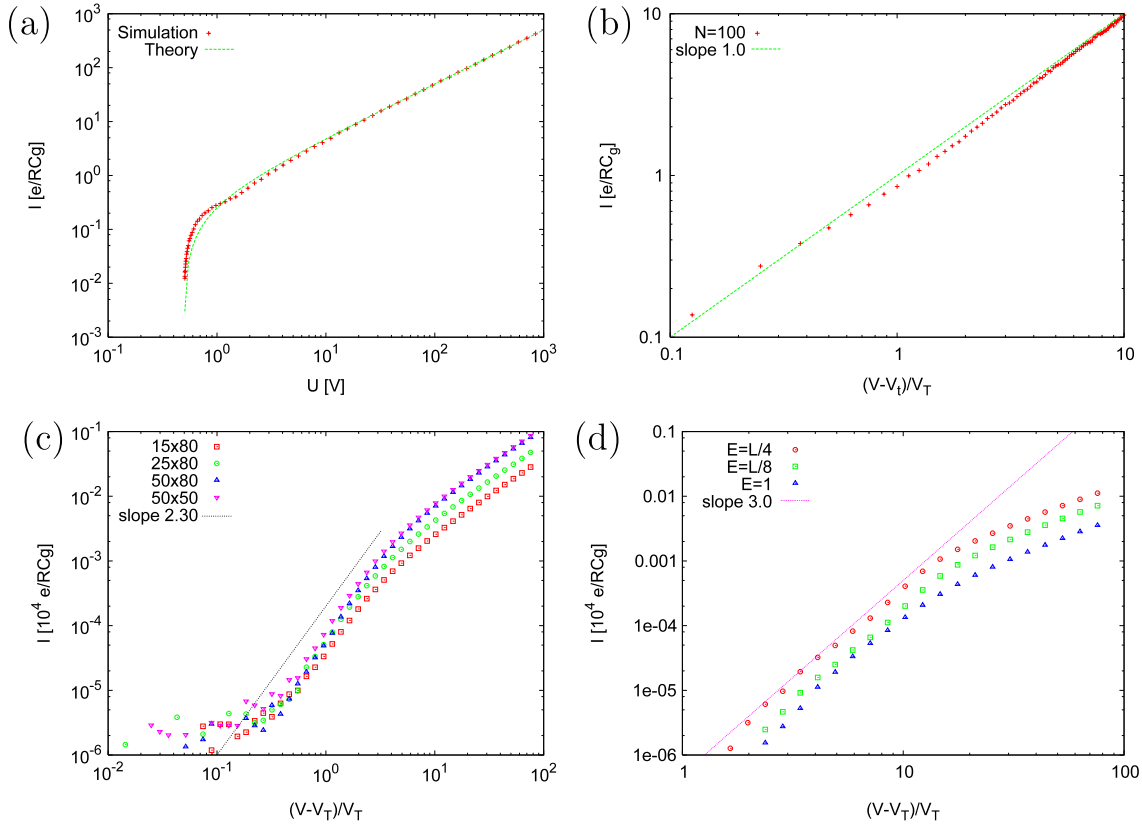
Figure 10. Simulated current–voltage curves for: (a) single nanoparticle between the electrodes and comparison with the exact expression in equation (26), shown by solid line; (b) linear chain of $N = 1000$ nanoparticles; (c) regular triangular array with quenched charge disorder and several sizes of sample; (d) regular hexagonal array of nanoparticles and several sizes of electrodes (the structure is shown in figure 4(c)).

of processed tunneling events. In the case when $C \ll C_g$ the algorithm can be simplified by neglecting the off-diagonal elements beyond the nearest-neighbor ones, as discussed above. Then a number of $O(N)$ operations per each tunneling is needed, reducing the complexity of the whole algorithm to $O(N^3 + MN)$.

Within the numerical implementation of the tunneling processes introduced above, different types of nanoparticle assemblies and realistic situations can be adequately taken into account. In particular:

- *Topological disorder* is included in the adjacency matrix of the nanoparticle network;
- *Charge disorder*, seen as the offset charges at nanoparticles, is incorporated by preparing a vector of quenched charges $0 \leqslant q_i < e$ from a uniform random distribution. It shifts the actual charge at a nanoparticle as $Q_i \rightarrow Q_i + q_i$, thus changing the local charge/voltage balance and affecting the tunneling condition;
- *Temperature effects* on the tunneling rate Γ_{ij} are included in the expression (17);
- *Capacitance variations* at the local level, i.e., due to different sizes (and capacitances) of each nanoparticle can be taken, for instance with a Gaussian distribution around an average C. Also, various limits beyond the familiar $C \ll C_g$ can be studied;
- *Quantum resistance variations*, i.e., due to different types of linkers between individual nanoparticles in the

assembly, or variations in the distances (distribution of the tunneling radius), can be easily implemented and their effects analyzed.

In this work we focus on the most striking features occurring due to the topology of the nanoparticle films and on comparison between the topological and charge disorder. For this purpose, we set the temperature to zero, which simplifies the expression (17) to

$$\Gamma_{i \rightarrow j}(V) = \frac{1}{e^2 R_{t, i \rightarrow j}} \Delta E_{i \rightarrow j}. \tag{56}$$

To speed up the algorithm we often consider the case $C \ll C_g$ (see also [61, 75, 58, 60]).

4.2. Benchmarks and regular arrays

The numerical model is first tested with a few benchmark calculations, i.e., conduction through a single nanoparticle between the electrodes (cf figure 3) and an 1D nanoparticle array. We also compute the $I(V)$ curves for two regular 2D structures (the results are shown in figure 10): the triangular super-lattice, and a hexagonal nanoparticle array, which are useful for comparisons with the more general structures studied later in section 5. In all calculations we assume that $R, C, and\ C_g$ are constant and that $\Phi^- = \Phi^{\text{gate}} = 0$, while $\Phi^+ = V$. We also fix the ratio $C/C_g = 10^{-4}$, so the condition $C \ll C_g$ is well satisfied.

For simplicity, the capacitance between electrodes and the neighboring nanoparticles is assumed to be equal to the interparticle capacitance C. A uniform random distribution of the charge disorder is assumed in the case of the triangular array, corresponding to the situation in the experiment studied in [54]. Note that the characteristic timescale in this stochastic process is given by RC_g, so the current in our simulations is suitably expressed in the units of e/RC_g.

In the case of a single nanoparticle connected with tunneling junctions to both electrodes and capacitively coupled with the gate electrode, as shown in the figure 3, the simulated $I(V)$ curve is in full agreement with the theoretical prediction in equation (26). The curve is linear beyond the threshold voltage. A linear behavior is also obtained in the case of a 1D nanoparticle array, as expected. In figure 10(b) we show the dependence of the current I on the reduced voltage $(V - V_T)/V_T$, where V_T is the threshold voltage. In this case we find $V_T \sim N$, the number of nanoparticles in the chain.

In the other two benchmark cases shown in figures 10(c) and (d) nontrivial effects of both the $2D$ structures and the charge disorder are demonstrated. The case of the regular triangular array with charge disorder, shown in figure 10(c), represents the typical form of the $I(V)$ curve, which we will find in many situations in section 5. Three regions with different conduction regimes are visible: small noise below the threshold voltage V_T, a nonlinear regime for a range of voltages $V \gtrsim V_T$, and eventually bending towards a linear conduction regime for very large voltages. In this case the nonlinear regime can be fitted by the equation (1) with the exponent $\zeta \approx 2.3$, in good agreement with the experiment in [54]. We simulated different sample sizes $\ell_E \times \ell_S$, as indicated in the legend, where ℓ_E and ℓ_S are the length along the electrodes and the distance between the electrodes, respectively. As figure 10(c) shows, the size of the system slightly affects the slope of the curve above the threshold, however, the nonlinear region persists. In the case of the regular hexagonal structure *without charge disorder* the results show nonlinear curves with an even larger exponent $\zeta \approx 3$. The different curves here are for point electrodes ($E = 1$) and another two lengths of electrodes, expressed as the fraction of the perimeter E/L, indicated in figure 10(d).

5. Single-electron conduction in classes of nanoparticle networks

In this section and in section 6 we apply our numerical model to simulate the charge transport in complex structures of nanoparticle films, represented by nano-networks. Besides the topology of the networks, the emphasis is on the underlying long-range correlations which lead to the nonlinearity in the $I(V)$ curves. Specifically, we consider in parallel two types of network structures described here.

- Plane-filling cellular network (CNET), grown with the rules described in section 3.1, with parameters $\nu = 1$ and $\mu_2 = 0.5$. This type of network has weak topological disorder in view of the small dispersion of cell sizes around the hexagonal structure. In addition, they are locally homogeneous, namely each node in the interior

of the network has exactly three links (possible ways of path branching). These networks are also suitable to study charge disorder effects. For this case, a uniformly quenched distributed random charge $0 \leqslant q_i < 1$ is associated to each node in the network between the electrodes.
- Two networks named NNET1 and NNET2, shown in figure 7, representing nanoparticle films made by the evaporation methods, as described above. These networks have an inhomogeneous local structure with different dispersions of the number of links per node (cf insets to figures 12) and various degrees of topological disorder at large scale, which is related to the nanoparticle coverage.

All simulations are done under the same conditions as described in the case of benchmarks. The results for the $I(V)$ curves are always presented on a double-logarithmic plot with a suitably normalized current and the reduced voltage $(V - V_T)/V_T$, where the threshold V_T refers to each particular network. In these plots the nonlinearity exponent ζ is immediately identified by the slope of the $I(V)$ curve for $V \gtrsim V_T$. We first show the simulation results for the $I(V)$ curves and identify relevant conduction paths in these networks. Further analysis of the conduction process is done in section 6.

5.1. $I(V)$ characteristics in nanoparticle networks

The current–voltage characteristics for the cell-aggregated network CNET *with* and *without* charge disorder are shown in figures 11(a) and (b). The simulations are done for two network sizes (the number of nanoparticles), $N = 1000$ and 2000. In each case two types of electrodes are considered: point electrodes and electrodes that extend over $1/8$th of the perimeter along opposite sides of the sample (see figure 13(a) below). It is clear that on the CNET structure the $I(V)$ dependence is nonlinear above the threshold. However, in the presence of charge disorder the exponent is considerably smaller, $\zeta \approx 1.33$, compared with $\zeta \approx 2.5$ obtained on the same network without charge disorder. The system size and the size of the electrodes, on the other hand, do not have profound effects on the $I(V)$ curves.

In figures 12(a) and (b) are shown the I–V characteristics obtained by simulations of the charge transport *without charge disorder* on two nanoparticle film networks, NNET1 and NNET2. In these networks, originating from different nanoparticle coverages, topological differences occur both on the local and global scale. Specifically, these are the dispersions of the number of links per node, as shown in the insets to figures 12, as well as the global measure of path lengths and the centrality, shown in figure 8. These topological features appear to affect the conduction processes on these networks, leading to different ζ exponents, as well as other characteristics studied in section 6. The strong topological inhomogeneity in the case of NNET1, yields larger nonlinearity exponent $\zeta \approx 3.9$, which is in good agreement with the experimental results obtained in nanoparticle films prepared with non-equilibrium evaporation methods [58]. On the other hand, for the more homogeneous structure of NNET2,
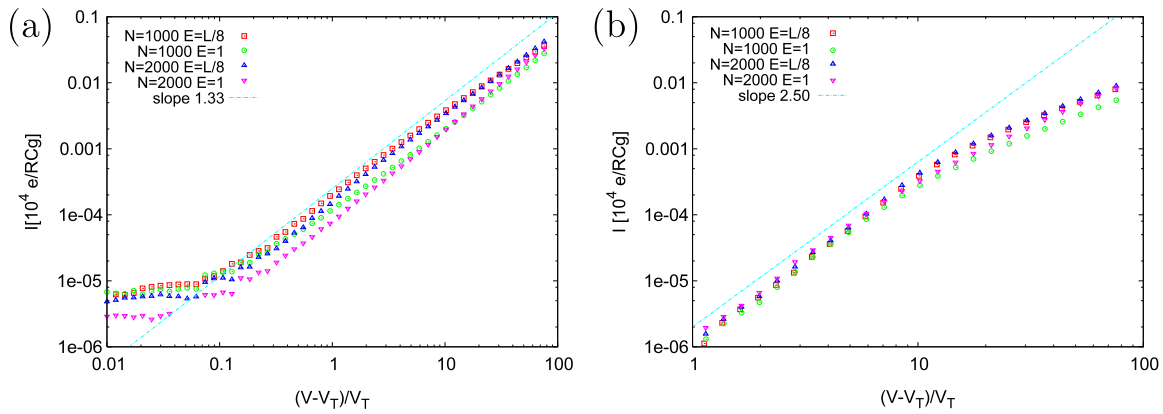
Figure 11. Simulated $I(V)$ curves for the cell-aggregated nanoparticle network CNET (a) with random charge disorder; (b) the same network without charge disorder. Symbols indicate the two sizes of the networks and the electrodes, as explained in the text.
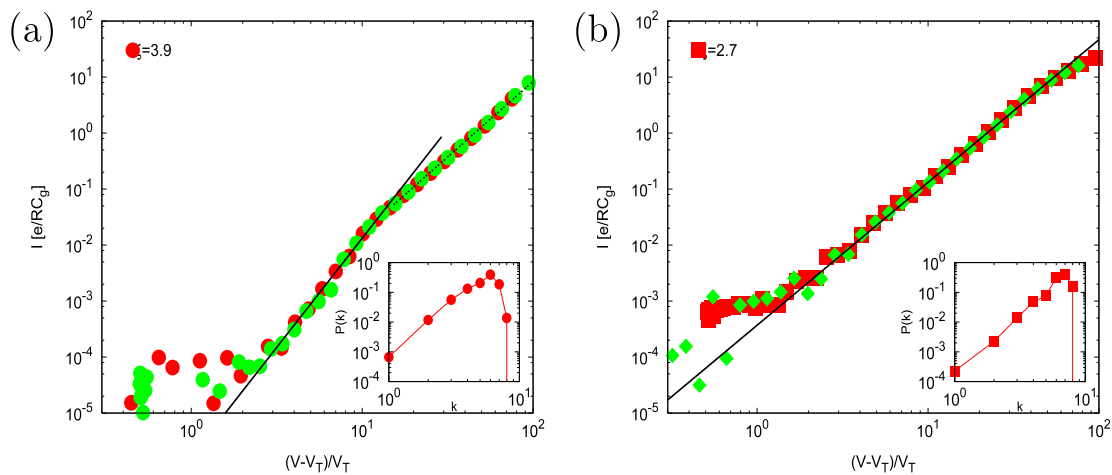

Figure 12. Simulated $I(V)$ curves on the nanoparticle film networks (a) NNET1, and (b) NNET2. The network structures are shown in figure 7. Insets: distributions of the number of links per node. (Data replotted from [58].)

we find the exponent $\zeta \approx 2.7$, more similar to the case of regular arrays without charge disorder studied above (see section 4.2). However, it is interesting to note that the range of relative voltages where the nonlinearity can be observed is by an order of magnitude smaller in the strongly inhomogeneous network.

5.2. Geometry of the conduction paths

In our model the electron tunnelings inside the sample occur simultaneously, driven by the voltage. When the current is established through the sample, however, the nature of charge flow changes. In this regime, the charge flow is mainly contained in several most important channels (conduction paths). Within our numerical model such paths can be identified on the nanoparticle network, and their topological and dynamical properties studied in detail. The number of electrons that tunnel along each junction on the network is monitored. This quantity is defined as the *flow*, f_{ij}, at the junction (i, j). Then the sequences of the junctions which carry most of the charge between the electrodes are found. Their geometry strongly depends on the topology of the underlying nanoparticle network and on the size and position of the electrodes. For instance, in figures 13(a) and (b) such

paths are visualized with thicker/darker lines in the case of the cellular network CNET with the point-like electrodes, and in the nanoparticle network NNET1 with the extended electrodes. The number of conduction paths increases and the merging of paths occurs with a further increase of the voltage. The charge flow at the end point of a particular channel affects the number of connected channels behind it, causing a larger area to drain along that channel. Consequently, the current increases beyond the linear $I(V)$ dependence. Hence, the geometry and the dynamics along the conduction paths are crucial for single-electron conduction in these systems.

The topology of the conduction paths is closely related to that of shortest paths, or 'topological flow', studied above (cf figure 8). In fact, the first channels to open at the threshold voltage coincide with the shortest paths between the actual positions of the electrodes. However, for $V \gtrsim V_T$ the dynamical (charge) flow differs from the topological flow in view of the merging paths, as mentioned above, and to opening of next-to-shortest paths, etc, when the voltage increases above V_T. A way to analyze the structure of the flow paths is to construct the *maximum flow spanning tree* [75] of the network. By definition, it is a spanning tree of the network with links $\{f_{ij}\}$, in which each node is connected to the tree by its largest flow link. In figures 14(a) and (b) we show the maximum flow
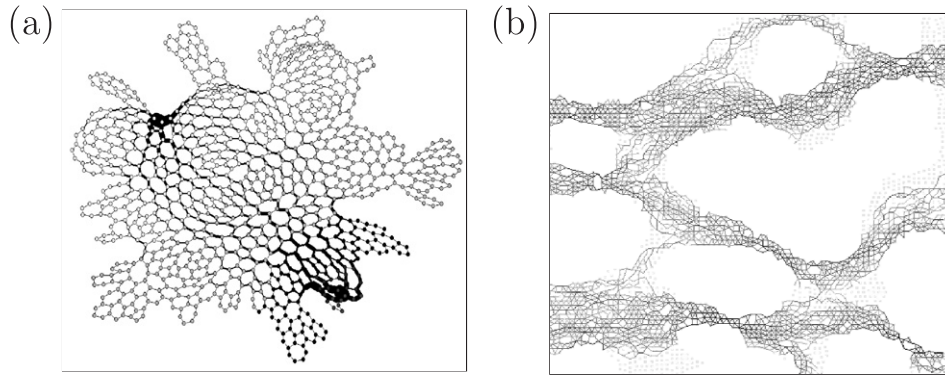
Figure 13. Conduction paths through the nanoparticle networks: (a) CNET with point-like electrodes; (b) NNET1 with line electrodes along the left and right boundaries. (Figure (b) reprinted with permission from [58]. ©2007, American Chemical Society.)
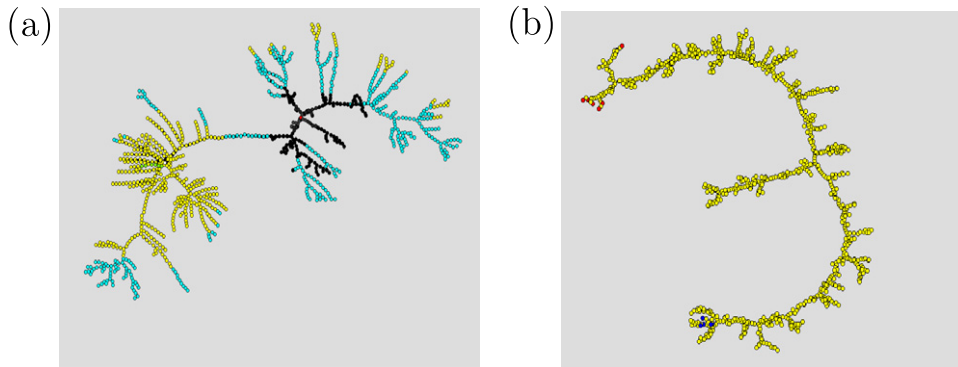

Figure 14. Maximum charge flow spanning trees for: (a) CNET with point electrodes, different voltage areas marked by colors; (b) part of the NNET1 including the main channel, electrodes are marked with different dark colors.

spanning tree for the CNET, and for the upper third part of the NNET1. In contrast to the topological flow (not shown), the charge flow trees appear to have a more linear structure, due to the dominant role of the electrodes. Notably, the most important nodes in this process are placed along the backbone of the tree.

6. Collective dynamical effects in the tunneling processes on networks

In this section we further investigate the properties of the conduction process along the conducting paths through the networks CNET and NNET1 (figure 13). In particular, we consider the time series of the dynamic activities at each node (nanoparticle) and each link (junction between nanoparticles). Defining several dynamical quantities, such as the charge flow along individual junctions, the tunneling delay, and the charge fluctuations on an individual nanoparticle and in the whole sample, we investigate the local properties and long-range correlations of the charge transport in these nanoparticle networks.

6.1. Charge flow distribution

The charge flow f_{ij}, mentioned above, is precisely defined as the net number of electrons through the junction (i, j) in a time window T_{win}. Specifically, for a given time window T_{win} the $f_{i \to j}$ and $f_{j \to i}$ are the number of electrons which tunnel

between the nanoparticles i and j in the direction of the arrow, then the net charge flow through the link (i, j), its 'dynamical betweenness centrality', is given as

$$f_{ij} \equiv |f_{i \to j} - f_{j \to i}|. \tag{57}$$

The flow is computed for all junctions $\{(i, j)\}$ on the network, and the distribution $P(f_{ij})$ of the flow for both networks are shown of figures 15(a) and (b). In both cases a broad distribution is found, indicating uneven flow along different links on the network. Apart from the region of small flow values, both distributions can be fitted with the q-exponential form

$$P(X) = B_q \left[1 - (1 - q) \frac{X}{X_0} \right]^{-1/(1-q)}, \tag{58}$$

which is often found in non-ergodic dynamical systems [79]. Note that the q-exponential form (58) in the limit of large values of the variable X gives a power-law decay with the exponent $\tau \equiv 1/(1 - q)$. The limit $q \to 1$ corresponds to the exponential function. The fit parameters for the flow distribution in the case of the cellular network CNET are: $B_Q = 2$, $X_0 = 100$, and $q = 1.25$, hence $\tau = 4.0$. For the nanoparticle network NNET1 we find: $B_Q = 80$, $X_0 = 35$, and $q = 1.14$, corresponding to the exponent $\tau = 7.0$.

6.2. Tunneling recurrence times

Another dynamical measure of the tunneling processes is the statistics of time intervals Δt between two successive
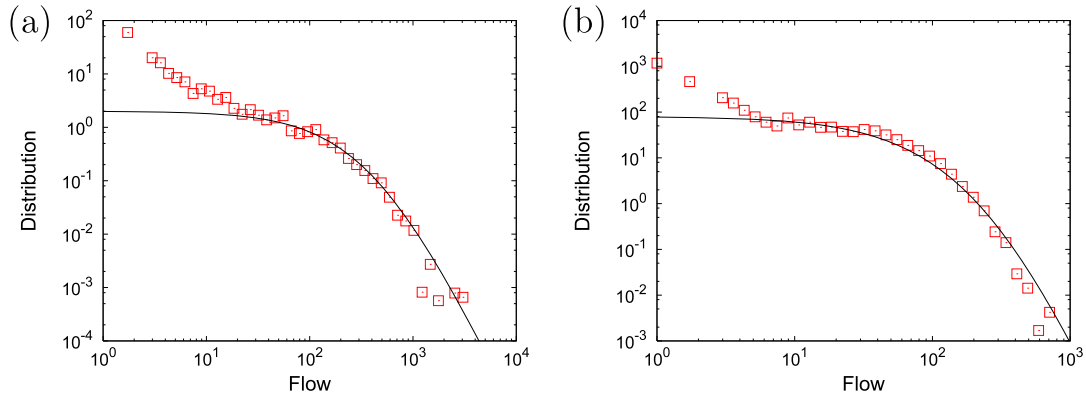
Figure 15. Distribution of charge flow along the links (dynamical betweenness) averaged over all links in the network for (a) CNET and (b) NNET1. Fit lines according to equation (58), see the text for details. (Data in figure (b) from [60].)
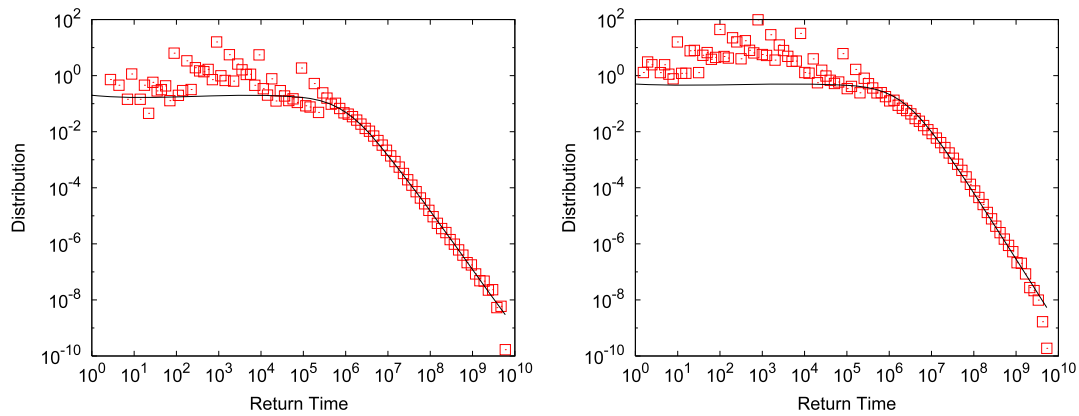

Figure 16. Distributions of time intervals Δt between two successive tunnelings at a node (first-return-times) $P(\Delta t)$, averaged over the network. Fits according to equation (58) (a) CNET, (b) NNET1. (Log-binned data.)

tunnelings at a given nanoparticle. In strongly correlated dynamical systems, such as earthquakes [80–82], critical sandpiles [83, 84] and financial market dynamics [85, 86], for example, the distribution of the time intervals (referred to as first return times, recurrence times, or waiting times) exhibits a power-law tail, compatible with the long-range correlations between the events.

In the simulations of the single-electron tunnelings in the nanoparticle networks CNET and NNET1, we monitor tunnelings at each nanoparticle in the system. The distribution $P(\Delta t)$ of the time intervals between successive tunnelings is determined for a fixed voltage $V = 10V_T$ and averaged over all nanoparticles in the assembly. The results are shown in figures 16(a) and (b). In both networks CNET and NNET1, the distribution can be fitted with the q-exponential form in equation (58) for large time intervals Δt. The fit parameters are: $B_Q = 0.2$, $X_0 = 5 \times 10^5$, and $q = 1.48$ (or $\tau = 2.08$) for the cellular network CNET, and $B_Q = 0.5$, $X_0 = 1 \times 10^6$, and $q = 1.4$ with corresponding exponent $\tau = 2.5$, in the case of NNET1. These results indicate the occurrence of long-range correlations in the tunneling events within the areas, which drain along the conduction paths. The patterns of separate lines for $\Delta t < X_0$ indicate the number of most active channels established at that particular voltage.

6.3. Correlated charge fluctuations

Further insight into the nature of the charge transport is gained by considering the time series of the number of tunneling events and relating it to temporal charge fluctuations at each nanoparticle in the system and at the electrode. For both sample networks, CNET and NNET1, we simulate the conduction under fixed voltage above the threshold, $V = 10V_T$, and after a relaxation period we sample the time series. The charge fluctuation at a given nanoparticle i with time t is determined by the number of tunnelings $n_i(t)$ at that nanoparticle within a given time window T_{win}. We find that an appropriate time window can be taken as $T_{win} = 4.11/\langle\Gamma\rangle$ for CNET, and $T_{win} = 17.10/\langle\Gamma\rangle$ for NNET, relative to the average tunneling rate $\langle\Gamma\rangle$ in the network. The time series $\{n_i(t)\}$, $i = 1, 2, \ldots, N$ are sampled for each node (nanoparticle). The global noise signal $N_T(t)$ at the level of the whole network is then calculated as the sum:

$$N_T = \sum_{i=1}^{N} n_i(t). \tag{59}$$

The computed time series in our simulations for the two network types appear to be fractal (see figures 17 and 18). Consequently, their power spectra defined by the
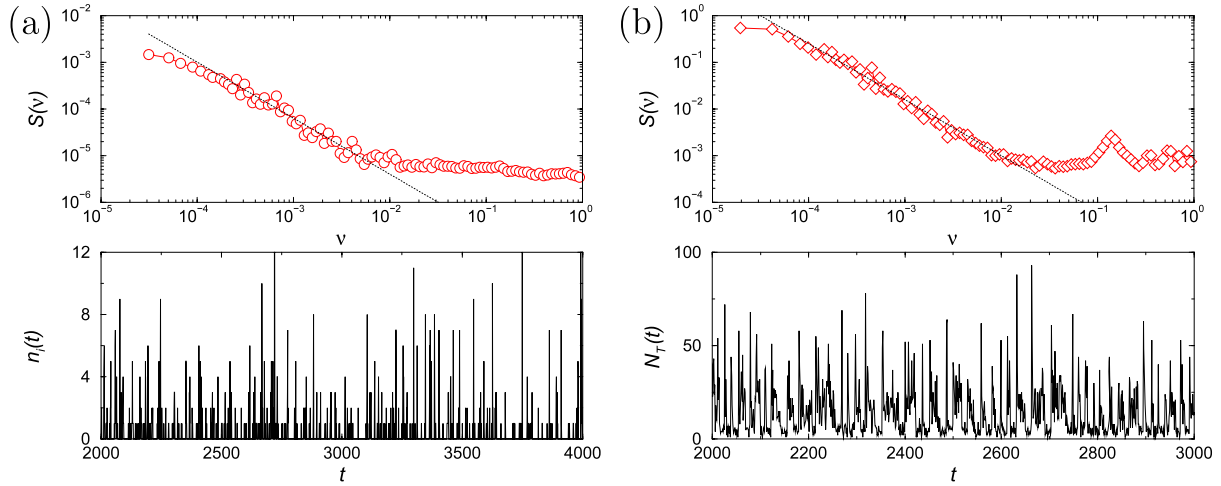
Figure 17. For the cellular network CNET: charge fluctuations time series (lower panels) and their power spectra (upper panels, log-binned data). Data corresponding to a single node (a) and to the whole network (b). Slopes: $\beta \simeq 1.2$ and 1.2.
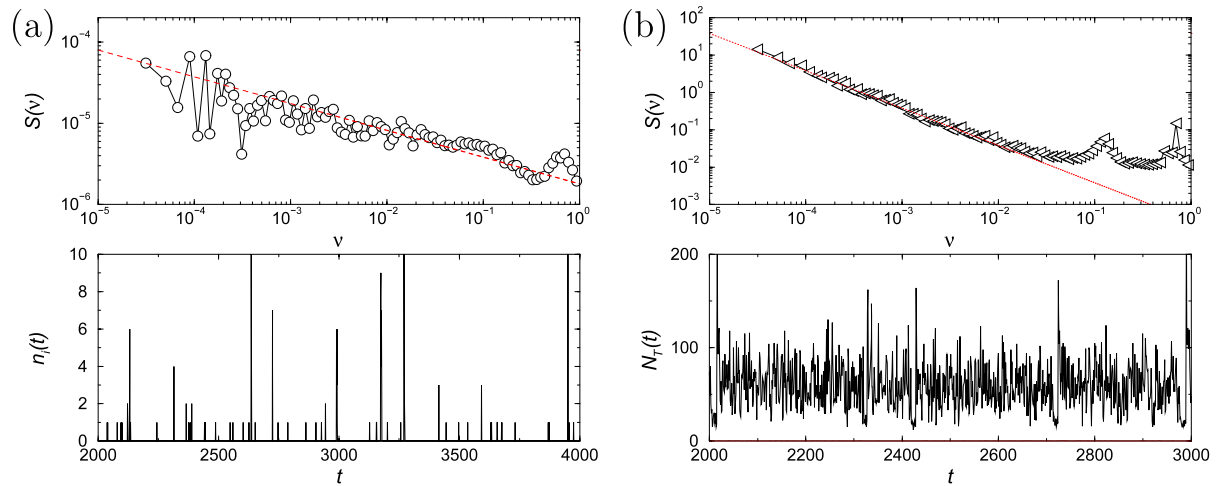

Figure 18. The same as figure 17, but for the nanoparticle network NNET1. Slopes: $\beta \simeq 0.33$ and 1.0. ((b) reprinted with permission from [60]. ©2009 IOP Publishing.)

expression (60), where N_s is the number of samples:

$$S(\nu) = \left| \sum_{j=0}^{N_s} n_j e^{i2\pi j\nu/N_s} \right|^2 \sim \nu^{-\beta}, \qquad (60)$$

exhibit a power-law dependence for a range of frequencies ν. The results in figures 17 and 18 show the time series and their spectra at two levels: at a single node inside the network (left panels) and the noise signal at the level of the whole network (right panels in both figures).

It is remarkable that, in the case of the almost regular cellular structure CNET, the correlations with the exponent $\beta \gtrsim 1$ already occur at a single nanoparticle inside the sample. The same exponent $\beta = 1.2$ (within error bars) is found for the global noise. This suggests that, once established, the geometry of conduction paths does not vary in this type of network structure (for fixed V). The situation is different in the nanoparticle network NNET1, which has strong topological inhomogeneity. Here the exponents of the power spectra at

the local and global level differ significantly. Specifically, weak correlations at a single nanoparticle lead to long-range correlations of $1/\nu$ type at the global level. In contrast to the case of cellular networks such as CNET, and other regular structures studied in [60], the appearance of long-range correlations in topologically inhomogeneous nano-networks, such as NNET1, indicates self-organized tunneling dynamics between different conduction paths.

Certain hidden patterns of the dynamical behavior of individual nodes on a complex network can be revealed by the analysis of the dispersion of the multichannel time series [87–89]. Here we consider the series $\{Q_i(t)\}$ of charge fluctuations, sampled at each node $i = 1, 2, \ldots, N$ in the network. They are closely related to the number of tunnelings $\{n_i(t)\}$ studied above, specifically, the charge $Q_i(t)$ at a nanoparticle i in a given time bin is determined by the difference between the number of incoming and the outgoing electrons at that particle within the time bin. Plotting the standard deviation of the time series against its average value
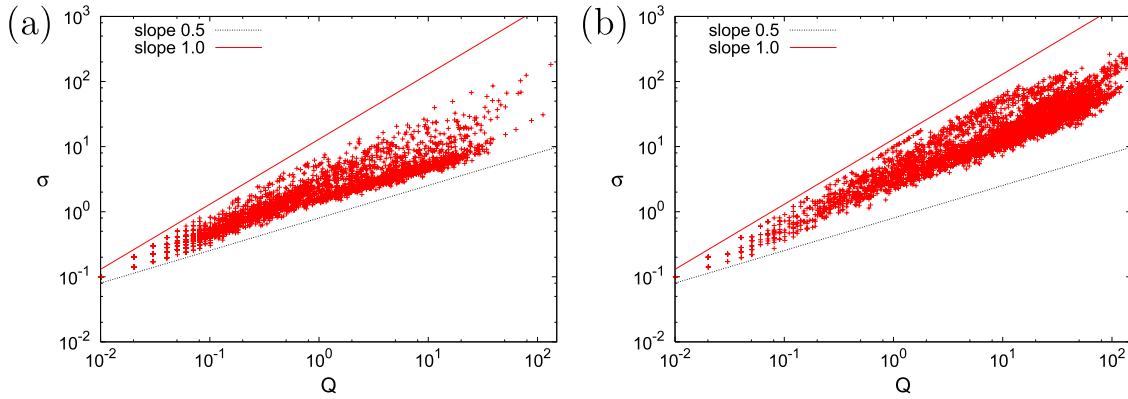
Figure 19. Scatter-plot of the standard deviations of the charge fluctuations time series on each nanoparticle plotted against the average charge on it. Each point represents one node (nanoparticle) in a network (a) CNET, with homogeneous connectivity of nodes, and (b) NNET1, with large topological inhomogeneity. Straight lines indicate the limiting slopes with $\mu = 1/2$ and 1 defined in equation (61).

for each node, a pattern is obtained which exhibits a well defined scaling law (see recent review with other different dynamical systems in [90] and references therein):

$$\sigma_i \sim \langle Q_i \rangle^\mu, \qquad (61)$$

with the exponent limited between two cases $\mu = 1/2$ and 1. The results for the two networks, CNET and NNET1, are shown in figures 19(a) and (b). In the case of the CNET structure, a large number of nodes align along the direction $\mu = 1/2$, compatible with the random fluctuations pattern, whereas in the inhomogeneous NNET1 a majority of nodes follow a pattern with driven dynamical behavior, with the exponent $\mu \approx 0.86$.

The long-range correlations in the charge fluctuations along the conduction paths through the network manifest themselves in the current which is measured at the electrode. In the simulations, we sample the time series of the current $\{I(t)\}$, which is precisely defined as the number of electrons arriving at the low-voltage electrode within a given time bin T_{win}. The temporal fluctuations in the current are induced both by the geometry of conduction paths through the network and charge fluctuations at nodes along these paths. Thus the increments of the current $\Delta I(t)$ between two consecutive time bins represent a suitable measure of the 'acceleration' of the tunnelings along the paths. We study the current fluctuations in the two network structures: NNET1 with strong topological disorder and, for comparison, a fully regular *triangular array of nanoparticles with charge disorder*. The current fluctuations time series in these two networks are shown in figure 20(a). The fractal structure of the time series is quantified in their power spectra (upper panel in the same figure). Again, the nature of the correlations in the charge fluctuations along the paths leads to different current correlations in these two network structures. Topological inhomogeneity contributes to long-range correlations in the current fluctuations at large frequencies, whereas only weak correlations can be detected the regular arrays and at low frequencies. The fluctuation patterns also affect the distribution of the current increments $P(\Delta I)$, shown in figure 20(b). The case of NNET1 shows that large bursts (both positive and negative) in the current

fluctuations are probable when the topology of the conduction paths varies. The distribution can be fitted with a q-Gaussian [91, 92]

$$P(\Delta I) = B_I \left[1 - (1-q) \left(\frac{\Delta I}{D_0} \right)^2 \right]^{-1/(1-q)}, \qquad (62)$$

often found in complex dynamical systems with long-range correlations, stock-market fluctuations and earthquake data analysis. The value for the parameter $q = 1.85$ fits the data in the case of NNET1, while for the triangular array with charge disorder $q = 1.14$ is much closer to the normal distribution, corresponding to the limit $q \to 1$.

7. Remark on the conduction in multiscale networks

In this work we presented a microscopic model of conduction with single-electron tunnelings through metallic nanoparticle networks, where the capacitive coupling is the dominant interaction. The tunneling junctions between nanoparticles in the model are characterized by the tunneling rate, Γ_{ij}, which is given by the *global* energy change following a single-electron tunneling through the junction ($i \to j$). In the numerical model the quantum tunneling resistance R_t appears as a relevant parameter which characterizes the junction. Here we briefly comment how this model can be used to estimate the structure effects on the conduction in more complex nanoparticle assemblies, in which the structure differs considerably at the local and mesoscopic scale.

In this respect, two types of inhomogeneity may arise. In the first, the junctions between all nanoparticles are equal, whereas the control parameters of the assembly processes vary, such that the global pattern differs from the local one, as in the theoretical examples in figures 4(a) and (b). A variety of such multiscale structures can be found in experiments with nanoparticle films prepared via evaporation methods (see [44] and references therein). The other type of inhomogeneity that we refer to is found when the linking between the nanoparticles is mediated by biomolecules, nanotubes, nanowires, etc. In this case the nanoparticle network (usually a small graph) can
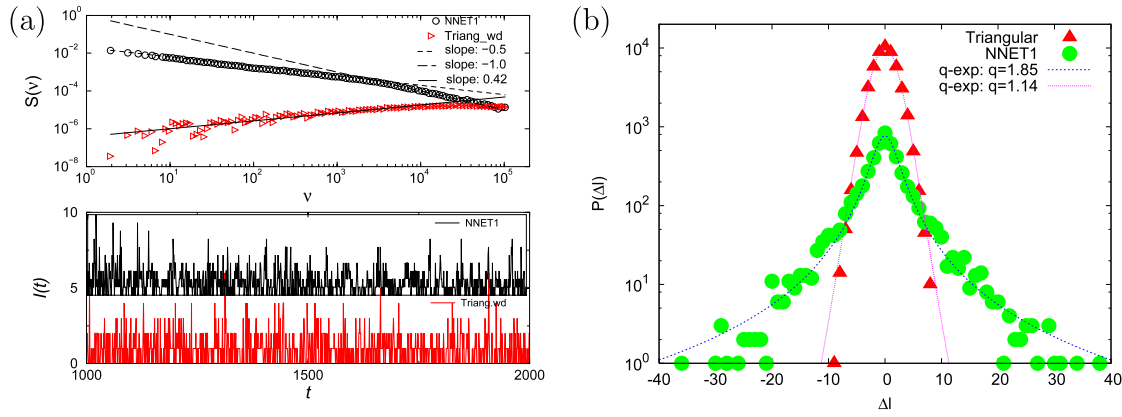
Figure 20. Time series of the current fluctuations $I(t)$ (a) and the distribution of current increments $P(\Delta I)$ plotted against ΔI for regular array of nanoparticles with charge disorder (triang-wd), and for topologically disordered nanoparticle network (NNET1). (Reprinted with permission from [60]. ©2009, IOP Publishing.)
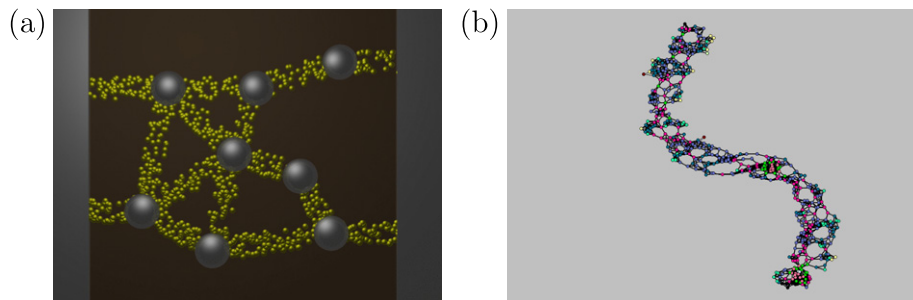

Figure 21. Computer generated multiscale structure with (a) a coarse-grained network, and (b) an isolated junction as a string of nanoparticles with different structure.

be quite homogeneous, however, the nature of the conduction along each complex junction could be different. The conductance (resistance) of each junction may be computed using microscopic theories, for example density functional theory [31] or other methods.

In the multiscale structure (an example generated numerically is shown in figures 21(a) and (b)), the conduction model can be applied at two levels: first at an individual junction, and then the results of each junction used as entries at the coarse-grained network. On the mesoscopic scale, the structure is represented by a simple graph marked with junctions and 'large' particles at the branching points. The coarse-graining topology is described by the adjacency matrix $A_{ij}^{(CG)}$. On a smaller scale, however, each junction consists of many particles with a particular spatial ordering, representing an effective resistor between the branching points of the coarse-grained network, see figure 21(b) as an example. Hence, the conduction properties along such a junction can be computed within our model of section 2.4, or using other methods appropriate for different types of junction. The results are the nonlinear $I_{ij}(V)$ dependence with a local exponent ζ_{ij} and a local value of the threshold voltage V_{ij} for each complex junction. Therefore, each link on a coarse-grained network can be characterized by a nonlinear current

$$I_{ij} \sim (V - V_{ij})^{\zeta_{ij}}, \tag{63}$$

depending on the microscopic structure of the junction. Now, assuming that the coarse-grained network can be treated

as a capacitively coupled system with effective (nonlinear) junctions, we can further apply the methods developed in the above sections to compute the conduction properties at the large scale. At each junction on the coarse-grained structure (i.e., between 'large' particles in figure 21(a)), we have a different tunneling rate, given by

$$\Gamma_{ij} = (\Phi_i - \Phi_j - V_{Tij})^{\zeta_{ij}}/e, \tag{64}$$

where $\Phi_i - \Phi_j$ is the potential difference between 'large' particles i and j. The vector of potential $\mathbf{\Phi}$ is defined by

$$\mathbf{\Phi} = \mathbf{M}_{(CG)}^{-1}\mathbf{Q} + \mathbf{M}_{(CG)}^{-1}\mathbf{C}_\mu\mathbf{\Phi}^\mu, \tag{65}$$

where the capacitance matrix for the coarse-grained structure is $\mathbf{M}_{(CG)}$.

The results of the simulations (not shown) suggest that the topology of the coarse-grained network may enhance the nonlinearity which is present at the local scale. For instance, starting with a constant exponent $\zeta_{ij} = 2.5$ as the nonlinearity exponent at each junction string and assuming the structure of the CNET type (see figure 4(b)) as a coarse-grained network, we find an increased exponent $\zeta = 2.8$ for the $I(V)$ curve at the global scale.

Self-similar cellular structures, such as the example shown in figure 1(d) and in [44], represent another interesting case, where the fractal patterns occur at different scales. From the point of view of the conduction, we expect that the broad distribution of voids occurring in these patterns will

affect the conduction paths and, thus, the scaling exponents. Mapping the known structure onto nanoparticle networks and implementation of the electron tunneling conduction, as described in this work, is entirely applicable to these type of structures, once the positions of the nanoparticles are inferred. For the theoretical analysis of the structure–conduction interdependences, however, modeling of the structure, e.g., via cellular-aggregation process as in section 3.1 could be useful. Within these models the quantitative control of the topology of the assembly is achieved through the control parameters. For instance, structures such as the one in figure 1(d) can be grown by planting several seeds for the branched aggregates with the parameter $\nu = 0$, and specified μ_2 (a special case with loop size $\ell = 1$ corresponds to aggregation of individual particles, leading to the DLA clusters).

The question remains how representative are these cellular network models in relation to real assemblies on substrates. Within this concept, a graph can be considered as the appropriate model of an assembly of nanoparticles if it takes into account the main topological features of the assembly which are relevant for conduction. In this work we have studied several examples where the topological properties of the network (betweenness centrality, connectivity, distribution of voids, etc) affect the conduction paths. It is an advantage of numerical modeling that such topological properties can be varied in a controlled manner within the network models, and a wide range of parameters exploited and compared with experimental situations.

8. Conclusion

In the conducting nanoparticle films a line of crucial interdependences: *assembly processes* $\Rightarrow$ *emergent structures* $\Rightarrow$ *emergent physical properties* needs to be systematically observed in both research and technology applications. Here we have reviewed charge transport via single-electron tunneling mechanisms in nanoparticle films of various structures within a numerical modeling approach, which is in many ways complementary to the laboratory measurements. Within our approach the quantitative studies of the structure–dynamics interdependences are made possible by suitable mapping of the nanoparticle films onto networks and then using graph theoretical methods and simulations of the charge transport on them. Besides predicting the behavior of the measurable quantities (e.g., current at the electrodes), the numerical approach reveals the collective nature of the transport process inside the system, in particular along the dynamical conduction paths, which lead to the current–voltage nonlinearity.

In simulations with several types of nanoparticle network we focused on the role of *topological disorder* and, for comparison, *quenched charge disorder* on single-electron tunneling conduction. Our results suggest that two major classes of conduction behavior can be identified, depending on the global network topology and the presence of charge disorder. Specifically:

- *Regular cellular and close-packed nanoparticle structures*, exhibiting moderately high nonlinearity in the $I(V)$ curves. For instance $\zeta \approx 3$ for the hexagonal cellular network without charge disorder. In the presence of weak

topological disorder, i.e., dispersion of the cell sizes, or the number of links per node in close-packed networks, the exponent is slightly reduced, $\zeta \approx 2.5$–2.8. However, a strong reduction of the nonlinearity is found in the presence of quenched charge disorder, $\zeta \approx 1.3$ found in these networks. $\zeta \approx 2.3$ in regular triangular arrays, in agreement with the experiment [54]. In these network structures the conduction paths for $V \geqslant V_T$ have a practically fixed geometry. This is compatible with the observed charge fluctuations, with an equal degree of correlations at the local and the global level, and strong blocking effects of the charge disorder along the individual paths.

- *Nanoparticle networks with strong topological inhomogeneity*, manifested in the power-law tail in the distribution of the betweenness centrality measure and a dispersion in the node degree, belong to another class of conduction with very large $I(V)$ nonlinearity. The exponent $\zeta \approx 3.9$ is found in the NNET1, comparable with the experimental results [58]. The nonlinearity in these network structures occurs in a smaller range of voltages, compared to the regular structures, and it is related to strong correlations in the charge fluctuations between different dynamically varying conduction paths.

Topologically inhomogeneous nanoparticle networks, such as the NNET1 in our study, represent a new class of conducting nanoparticle films with strong collective dynamical effects. The simulations demonstrate that correlations in the charge fluctuations are systematically built from the individual nanoparticles to the paths and the whole network, leading eventually to large bursts of measurable current at the electrode. Direct measurements of the charge fluctuations might be difficult. However, their effects in the time series of the current fluctuations at the electrode can be directly measured (such measurements have been recently reported in the case of nanowires [93]). Our results suggest that the two classes of conducting nanoparticle networks exhibit different distributions of their current fluctuations. In particular, collective charge transport is reflected in the appearance of 'wings' in the distribution of current increments, as opposed to a normal distribution in the regular nanoparticle structures.

We would like to stress that the potential of this model of capacitively coupled nanoparticle networks, with the numerical implementation described in sections 2 and 4, exceeds the cases studied in this work (see also [61]). In particular, the effects of thermal fluctuations, variations in distances between nanoparticles and their sizes, leading to a distribution of capacitances C_{ij}, and even different types of conduction through individual junctions can be studied along the same lines as presented here. Complementary to the experiments, the numerical studies of this type reveal how the conduction properties of the nanoparticle films emerge based on their structure.

Acknowledgments

coordinated by P Moriarty. We also acknowledge support by the National Program P1-0044 (Slovenia) and Project MNTRS 141025 (Serbia).

References

[1] Moriarty P 2001 Nanostructured materials *Rep. Progr. Phys.* **64** 297–381

[2] Di Ventra M, Evoy S and Heflin J R (ed) 2004 *Introduction to Nanoscale Science and Technology* (*Technology & Industrial Arts*) (Berlin: Springer)

[3] Scharff P and Buzaneva E (ed) 2004 *Frontiers Of Multifunctional Integrated Nanosystems* (Berlin: Springer)

[4] Dupas C, Houdy P and Lahmani M (ed) 2006 *Nanoscience: Nanotechnologies and Nanophysics* (Berlin: Springer)

[5] Narlikar A V and Fu Y Y (ed) 2010 *The Oxford Handbook of Nanoscience and Technology—Frontiers and Advances in Three Volumes* (Oxford: Oxford University Press)

[6] Bird J P (ed) 2003 *Electron Transport in Quantum Dots* (Berlin: Springer)

[7] Heinzel T 2003 *Mesoscopic Electronics in Solid State Nanostructures* (Weinheim: Wiley–WHC)

[8] Pelesko J A 2007 *Self-Assembly: the Science of Things that put Themselves Together* (Boca Raton, FL: Chapman and Hall/CRC)

[9] Nepomnyashchy A and Golovin A (ed) 2006 *Self-assembly, Pattern Formation and Growth Phenomena in Nano-systems* (Berlin: Springer)

[10] Murray C B, Kagan C R and Bawendi M G 2000 Synthesis and characterization of monodisperse nanocrystals and close-packed nanocrystal assemblies *Annu. Rev. Mater. Sci.* **30** 545–610

[11] Pileni M P 2001 Nanocrystal self-assemblies: fabrication and collective properties *J. Phys. Chem.* B **105** 3358–71

[12] Pileni M P 2007 Self-assembly of inorganic nanocrystals: fabrications and collective intrinsic properties *Acc. Chem. Res.* **40** 685–93

[13] Yin Y and Alivisatos A P 2004 Colloidal nanocrystal synthesis and the organic–inorganic interface *Nature* **437** 664–70

[14] Muševič I, Škarabot M, Tkalec U, Ravnik M and Žumer S 2006 Two-dimensional nematic colloidal crystals self-assembled by topological defects *Science* **313** 954–8

[15] Likos C N 2001 Effective interactions in soft condensed matter physics *Phys. Rep.* **348** 267–439

[16] Zaccarelli E 2007 Colloidal gels: equilibrium and non-equilibrium routes *J. Phys.: Condens. Matter* **19** 323101

[17] Storhoff J J and Mirkin C A 1999 Programmed materials synthesis with DNA *Chem. Rev.* **99** 1849–62

[18] Winfree E, Liu F, Wenzler L A and Seeman N C 1998 Design and self-assembly of two-dimensional DNA crystals *Nature* **394** 539–44

[19] Park S Y, Lytton-Jean A K R, Lee B, Weigand S, Schatz G C and Mirkin C A 2008 DNA-programmable nanoparticle crystallization *Nature* **451** 553–6

[20] Nykypanchuk D, Maye M M, van der Lelie D and Gang O 2008 DNA-guided crystallization of colloidal nanoparticles *Nat. Lett.* **451** 549–52

[21] Aldaye F A, Palmer A L and Sleiman H F 2008 Assembling materials with DNA as the guide *Science* **321** 1795

[22] Mirkin C A 2000 Programming the assembly of two- and three-dimensional architectures with DNA and nanoscale inorganic building blocks *Inorg. Chem.* **39** 2258–72

[23] Mirkin C A, Letsinger R L, Mucic R C and Storhoff J J 1996 A DNA-based method for rationally assembling nanoparticles into macroscopic materials *Nature* **382** 607–9

[24] Boal A K, Ilhan F, DeRouchey J E, Thurn-Albrecht T, Russell T P and Rotello V M 2000 Self-assembly of nanoparticles into structured spherical and network aggregates *Nature* **404** 746–8

[25] Heilmann A 2003 *Polymer Films with Embedded Metal Nanoparticles* (Berlin: Springer)

[26] Martin C P, Blunt M O and Moriarty P 2004 Nanoparticle networks on silicon: self-organized or disorganized? *Nano Lett.* **4** 2389–92

[27] Xia D, Li D, Luo Y and Brueck S R J 2006 An approach to lithographically defined self-assembled nanoparticle films *Adv. Mater.* **18** 930–3

[28] Blunt M O, Martin C P, Ahola-Tuomi M, Pauliac-Vaujour E, Sharp P, Nativo P, Brust M and Moriarty P J 2007 Coerced mechanical coarsening of nanoparticle assemblies *Nat. Nanotechnol.* **2** 167–70

[29] Alivisatos P 2004 The use of nanocrystals in biological detection *Nat. Biotechnol.* **22** 47–52

[30] Tadić B 2008 From microscopic rules to emergent cooperativity in large scale patterns *Systems Self-Assembly: Multidisciplinary Snapshots* (Amsterdam: Elsevier)

[31] Koskinen P, Hakkinen H, Seifert G, Sanna S, Frauenheim T and Moseler M 2006 Density-functional based tight-binding study of small gold clusters *New J. Phys.* **8** 9

[32] Zabet-Khosousi A and Dhirani Al-A 2008 Charge transport in nanoparticle assemblies *Chem. Rev.* **108** 4072–124

[33] Daniel M-C and Astruc D 2004 Gold nanoparticles: assembly, supramolecular chemistry, quantum-size-related properties and applications toward biology, catalysis and nanotechnology *Chem. Rev.* **104** 293–346

[34] Archer P I, Santangelo S A and Gamelin D R 2007 Direct observation of sp–d exchange interactions in colloidal Mn^{2+}- and Co^{2+}-doped CdSe quantum dots *Nano Lett.* **7** 1037–43

[35] Brust M, Walker M, Bethell D, Schiffrin D J and Whyman R 1994 Synthesis of thiol-derivatised gold nanoparticles in a two-phase liquid–liquid system *J. Chem. Soc. Chem. Commun.* **7** 801

[36] Brennan J *et al* 2006 Bionanoconjugation via click chemistry: the creation of functional hybrids of lipases and gold nanoparticles *Bioconjug. Chem.* **17** 1373–5

[37] Andres R P, Bielefeld J D, Henderson J I, Janes D B, Kolagunta V R, Kubiak C P, Mahoney W J and Osifchin R G 1996 Self-assembly of a two-dimensional superlattice of molecularly linked metal clusters *Science* **273** 1690–3

[38] Moriarty P, Taylor M D R and Brust M 2002 Nanostructured cellular networks *Phys. Rev. Lett.* **89** 248303

[39] Huang J, Kim F, Tao A R, Connor S and Yang P 2005 Spontaneous formation of nanoparticle stripe patterns through dewetting *Nat. Mater.* **4** 896–900

[40] Blunt M O, Martin C P, Pauliac-Vaujour E, Stannard A, Moriarty P, Vancea I and Thiele U 2007 Controlling pattern formation in nanoparticle assemblies via directed solvent dewetting *Phys. Rev. Lett.* **99** 116103

[41] Lee L-T, Leite A P and Galembeck F 2004 Controlled nanoparticle assembly by dewetting of charged polymer solutions *Langmuir* **20** 4430–5

[42] Kim B, Tripp L and Wei A 2001 Self-organization of large gold nanoparticle arrays *J. Am. Chem. Soc.* **123** 7955–6

[43] Lin J, Zhou W and O'Connor C J 2001 Formation of ordered arrays of gold nanoparticles from CTAB feverse micelles *Mater. Lett.* **49** 282–6

[44] Blunt M O, Stannard A, Pauliac-Vaujour E, Martin C P, Vancea I, Šuvakov M, Thiele U, Tadić B and Moriarty P 2010 Patterns and pathways in nanoparticle self-organization *The Oxford Handbook of Nanoscience and Technology* vol I (Oxford: Oxford University Press)

[45] Diao J J, Qiu F S and Reeves M E 2003 Surface vertical deposition for gold nanoparticle film *J. Phys. D: Appl. Phys.* **36** L25–7

[46] Alivisatos A P, Johnsson K P, Peng X, Wilson T E, Loweth C J, Bruchezjr M P and Schultz P G 1996 Organization of 'nanocrystal molecules' using DNA *Nature* **382** 609–11

[47] Rimberg A J, Ho T R and Clarke J 1995 Scaling behavior in the current–voltage characteristic of one- and two-dimensional arrays of small metallic islands *Phys. Rev. Lett.* **74** 4714–7

[48] Duruöz C I, Clarke R M, Marcus C M and Harris J S Jr 1995 Conduction threshold, switching and hysteresis in quantum dot arrays *Phys. Rev. Lett.* **74** 3237–40

[49] Ferry D K and Goodnick S M 1997 *Transport in Nanostructures* (Cambridge: Cambridge University Press)

[50] Bakhvalov N S, Kazacha G S, Likharev K K and Serdyukova S I 1991 Statics and dynamics of single-electron solitons in two-dimensional arrays of ultrasmall tunnel junctions *Physica* B **173** 319–28

[51] Middleton A A and Wingreen N S 1993 Collective transport in arrays of small metallic dots *Phys. Rev. Lett.* **71** 3198–201

[52] Wybourne M N, Clarke L, Yan M, Cai S X, Brown L O, Hutchison J and Keana J F W 1997 Coulomb-blockade dominated transport in patterned gold-cluster structures *Japan. J. Appl. Phys.* **36** 7796–800

[53] Geigenmuller U and Schon G 1989 Single-electron effects in arrays of normal tunnel junctions *Europhys. Lett.* **10** 765–70

[54] Parthasarathy R, Lin X and Jaeger H M 2001 Electronic transport in metal nanocrystal arrays: the effect of structural disorder on scaling behavior *Phys. Rev. Lett.* **87** 186807

[55] Parthasarathy R, Lin X, Elteto K, Rosenbaum T F and Jaeger H M 2004 Percolating through networks of random thresholds: finite temperature electron tunneling in metal nanocrystal arrays *Phys. Rev. Lett.* **92** 076801

[56] Elteto K, Antonyan E G, Nguyen T T and Jaeger H M 2005 Model for the onset of transport in systems with distributed thresholds for conduction *Phys. Rev.* B **71** 064206

[57] Reichhardt C and Olson Reichhardt C J 2003 Charge transport transitions and scaling in disordered arrays of metal dots *Phys. Rev. Lett.* **90** 046802

[58] Blunt M O, Šuvakov M, Pulizzi F, Martin C P, Pauliac-Vaujour E, Stannard A, Rushforth A W, Tadić B and Moriarty P 2007 Charge transport in cellular nanoparticle networks: meandering through nanoscale mazes *Nano Lett.* **7** 855

[59] Beverly K C, Sampaio J F and Heath J R 2002 Effects of size dispersion disorder on the charge transport in self-assembled 2d Ag nanoparticle arrays *J. Phys. Chem.* B **106** 2131–5

[60] Šuvakov M and Tadić B 2009 Collective charge fluctuations in single-electron processes on nano-networks *J. Stat. Mech.: Theory Exp.* P02015

[61] Šuvakov M 2009 Network models of self-assembled functional materials *PhD Thesis* International Postgraduate School 'Jožef Stefan'

[62] Cieplak M, Maritan A and Banavar J R 1994 Optimal paths and domain walls in the strong disorder limit *Phys. Rev. Lett.* **72** 2320

[63] Maritan A, Coloari F, Cieplak M and Banavar J R 1996 Universality classes of optimal channel networks *Science* **272** 984

[64] Tadić B 1998 Disorder-induced critical behavior in driven diffusive systems *Phys. Rev.* E **58** 168

[65] Wernsdorfer W, Bonet Orozco E, Hasselbach K, Benoit A, Mailly D, Kubo O, Nakano H and Barbara B 1997 Macroscopic quantum tunneling of magnetization of single ferrimagnetic nanoparticles of barium ferrite *Phys. Rev. Lett.* **79** 4014–7

[66] Guéron S, Deshmukh M M, Myers E B and Ralph D C 1999 Tunneling via individual electronic states in ferromagnetic nanoparticles *Phys. Rev. Lett.* **83** 4148–51

[67] Bezryadin A, Dekker C and Schmid G 1997 Electrostatic trapping of single conducting nanoparticles between nanoelectrodes *Appl. Phys. Lett.* **71** 1273

[68] Boccaletti S, Latora V, Moreno Y, Chavez M and Hwang D U 2006 Complex networks: structure and dynamics *Phys. Rep.* **424** 175–308

[69] Dorogovtsev S N and Mendes J F F 2003 *Evolution of Networks* (Oxford: Oxford University Press)

[70] Tadić B, Rodgers G J and Thurner S 2007 Transport on complex networks: flow, jamming and optimization *Int. J. Bifurcation Chaos* **17** 2363–85

[71] Tadić B and Thurner S 2005 Search and topology aspects in transport on scale-free networks *Physica* A **346** 183

[72] Šuvakov M and Tadić B 2006 Topology of cell-aggregated planar graphs *Computational Science—ICCS 2006* (*Springer Lecture Notes in Computer Science* vol 3993) ed V Alexandrov *et al* (Berlin: Springer) pp 1098–105

[73] Maillard M, Motte L, Ngo A T and Pileni M P 2000 Rings and hexagons made of nanocrystals: a Marangoni effect *J. Phys. Chem.* B **104** 11871–7

[74] Stavans J 1993 Evolution of cellular structures *Rep. Prog. Phys.* **56** 733–89

[75] Šuvakov M and Tadić B 2006 Transport processes on homogeneous planar graphs with scale-free loops *Physica* A **372** 354

[76] Bollobás B 1998 *Modern Graph Theory* (New York: Springer)

[77] Ahuja R K, Magnanti T L and Orlin J B 1993 *Network Flows: Theory, Algorithms and Applications* (Englewood Cliffs, NJ: Prentice-Hall)

[78] Rabani E, Geissler P L, Reichman D R and Brus L E 2003 Drying-mediated self-assembly of nanoparticles *Nature* **426** 271–4

[79] Tsallis C 1988 Possible generalization of Boltzmann–Gibbs statistics *J. Stat. Phys.* **52** 479

[80] Corral A 2004 Long-term clustering, scaling and universality in the temporal occurence of earthquakes *Phys. Rev. Lett.* **92** 108501

[81] Corral A 2005 Mixing of rescaled data and Bayesian interface for earthquakes recurrence times *Nonlinear process. Geophys.* **12** 89–100

[82] Corral A 2006 Universal earthquake-occurence jumps, correlation with time and anomalous diffusion *Phys. Rev. Lett.* **97** 17850

[83] Boguna M and Corral A 1997 Long-tail trapping times and Levy flights in a self-organized critical granular systems *Phys. Rev. Lett.* **78** 4950–3

[84] Sanchez R and Carreras B A 2002 Waiting-time statistics of self-organized criticality systems *Phys. Rev. Lett.* **88** 068302

[85] Sabatelli L, Keating S, Dudley J and Richmond P 2002 Waiting-time distributions in financial markets *Eur. Phys. J.* B **27** 273–5

[86] Lee J W, Lee E K and Rikvold P R 2006 Waiting-time distributions for a stock-market index *J. Korean Phys. Soc.* **48** 123–6

[87] Tadić B 2006 Structure of noise and flow in transport on complex networks *Prog. Theor. Phys. Suppl.* **162** 112–20

[88] Živković J, Tadić B, Wick N and Thurner S 2006 Statistical indicators of collective behavior and functional clusters in gene expression networks of yeast *Eur. Phys. J.* B **50** 255–8

[89] Kujawski B, Tadić B and Rodgers G J 2007 Preferential behaviour and scaling in diffusive dynamics on networks *New J. Phys.* **9** 154

[90] Eisler Z, Bartosand I and Kertsz J 2008 Fluctuation scaling in complex systems: Taylor's law and beyond *Adv. Phys.* **57** 89–142

[91] Pluchino A, Rapisarda A and Tsallis C 2008 A closer look at the indications of q-generalized central limit theorem behavior in quasi-stationary states of the hmf model *Physica* A **387** 3121

[92] Tsallis C, Rapisarda A, Pluchino A and Borges E P 2007 On the non-Boltzmannian nature of quasi-stationary states in long-range interacting systems *Physica* A **381** 143

[93] Kohno H and Takeda S 2007 Non-Gaussian fluctuation in the charge transport of Si nanochains *Nanotechnology* **18** 359706